Solid Earth Discuss., 6, 1799–1861, 2014
www.solid-earth-discuss.net/6/1799/2014/
doi:10.5194/sed-6-1799-2014

Solid Earth Discussions
Open Access

Finite lattice distortion patterns in plastically deformed zircon grains

E. Kovaleva[1], **U. Klötzli**[1], **G. Habler**[1], **and E. Libowitzky**[2]

[1]Department of Lithospheric Research, Faculty of Earth Sciences, Geography and Astronomy, University of Vienna, Althanstrasse 14, 1090 Vienna, Austria
[2]Department of Mineralogy and Crystallography, Faculty of Earth Sciences, Geography and Astronomy, University of Vienna, Althanstrasse 14, 1090 Vienna, Austria

Received: 27 June 2014 – Accepted: 8 July 2014 – Published: 25 July 2014

Correspondence to: E. Kovaleva (elizaveta.kovaleva@univie.ac.at)

Published by Copernicus Publications on behalf of the European Geosciences Union.

Abstract

This study examines finite deformation patterns of zircon grains from high-temperature natural shear zones. Various zircon-bearing rocks were collected in the Western Tauern Window, Eastern Alps, where they were deformed under amphibolite facies conditions, and in the Ivrea-Verbano Zone (IVZ), Southern Alps, where deformation is related with granulite-facies metamorphism. Among the sampled rocks are: granitic orthogneisses, meta-lamprophyres and paragneisses, all of which are highly deformed.

The investigated zircon grains ranging from 10 to 50 microns were studied in situ using a combination of scanning electron microscope (SEM) techniques, including secondary electron (SE), backscattered electron (BSE), forward scattered electron (FSE), cathodoluminescence (CL) imaging, and crystallographic orientation mapping by electron backscatter diffraction analysis (EBSD), as well as micro-Raman spectroscopy. Energy-dispersive X-ray spectrometry (EDS) was applied to host phases.

Microstructural analysis of crystal-plastically deformed zircon grains was based on high-resolution EBSD maps. Three general types of finite lattice distortion patterns were detected: Type (I) is defined by gradual bending of the zircon lattice with orientation changes of about 0.6° to 1.4° per µm without subgrain boundary formation. Type (II) represents local gradual bending of the crystal lattice coupled with the formation of subgrain boundaries that have concentric semicircular shapes in 2-D sections. Cumulative grain-internal orientation variations range from 7° to 40° within single grains. Type (III) is characterized by formation of subgrains separated by a well-defined subgrain boundary network, where subgrain boundaries show a characteristic angular closed contour in 2-D sections. The cumulative orientation variation within a single grain ranges from 3° to 10°. Types (I) and (II) predominate in granulite facies rocks, whereas type (III) is restricted to the amphibolite facies rocks.

Investigated microstructures demonstrate that misorientation axes are usually parallel to the ⟨001⟩ and ⟨100⟩ crystallographic directions; dominant slip systems operating along tilt boundaries are ⟨010⟩{001}, ⟨010⟩{100} and ⟨001⟩{010}. In case of twist bound-

SED

6, 1799–1861, 2014

aries the slip systems ⟨010⟩{001} and ⟨100⟩ {001} are active, whereas in some grains cross-slip takes place. This study demonstrates that activation of energetically preferable slip systems is mostly controlled by the degree of coupling with the host phase and by the viscosity ratio between inclusion and host, and defined by crystallographic and elastic anisotropy of the zircon lattice.

1 Introduction

1.1 Zircon and its significance in geosciences

Zircon is one of the most stable, and abundant accessory phases in many rock types. Due to its chemical stability and ability to incorporate and preserve radioactive uranium and rare earth elements (REE) zircon is widely used for isotopic mineral dating, as well as for the geochemical characterization of its forming environment (e.g. Davis et al., 2003; Reddy et al., 2007). Relatively high temperatures are required for significant volume diffusion of the trace cations in a pristine zircon crystal. For example, at 850 °C, a volume diffusion length of 5 µm would require about 10 million years for Pb, 1 billion years for Dy, and tens of billions of years for Ti (Cherniak and Watson, 2003). However, at lower temperatures, other diffusion mechanisms have been documented in natural samples, especially so-called "Pb loss", which is not consistent with experimental predictions for volume diffusion (e.g. Geisler et al., 2002). In the past, the common explanation for low-temperature diffusion in zircon was the effect of self-irradiation that causes metamictization and thus induces/enhances volume diffusion (Cherniak et al., 1991; Cherniak and Watson, 2003). Recently, a number of authors have found evidences for increased trace element diffusion in zircon due to crystal-plastic deformation (Flowers et al., 2010; MacDonald el al., 2013; Moser et al., 2009, 2011; Piazolo et al., 2012; Reddy et al., 2006, 2007, 2009; Reddy and Timms, 2010; Timms and Reddy, 2009; Timms et al., 2011, 2012). These authors have shown that crystal-plastic deformation of the crystal lattice can dramatically affect the content of

SED
6, 1799–1861, 2014

trace elements in zircon domains and, therefore, can cause isotopic system resetting. Deformation microstructures such as, for example, subgrain boundaries, formed by dynamic recrystallization, may act as fluid migration and fast element-diffusion pathways that cause local variations in the chemical and isotopic compositions of grains (Timms et al., 2006, 2011). However, so far there were only a few documentations of these phenomena presented in the literature mentioned above. Until now we have no clear understanding how and in which cases crystal-plastic deformation of zircon affects the interpretation of radiometric age data. Therefore it is important to decipher the controlling mechanisms and general features of zircon lattice distortion that may cause enhanced material transport through the crystal. The current study aims to classify and characterize different finite crystal-plastic deformation patterns of zircon found in natural rocks by comparing samples from different metamorphic environments and from various associations of hosting major phases.

1.2 Targeted material

All previous detailed microstructural analyses on crystal-plastic deformation of zircon crystals have focused on unusually large zircons, up to few millimeters in length, from uncommon occurrences (Moser et al., 2009, 2011; Piazolo et al., 2012; Reddy et al., 2006, 2007, 2009; Reddy and Timms, 2010; Schwartz et al., 2010; Timms and Reddy, 2009; Timms et al., 2011, 2012). In addition, some of the above mentioned studies examined embedded zircon grains that were extracted from the sample by heavy mineral separation (e.g. Moser at al., 2011; Reddy et al., 2009; Schwartz et al., 2010; Timms and Reddy, 2009; Timms at al., 2006). During the conventional procedure of extracting larger grains by classical mineral separation techniques the context of host minerals and the immediate environment is lost, which restricts interpretations and conclusions. Furthermore, deformed grains may be selectively destroyed during sample crushing and sieving.

In contrast with previous studies, the current work presents new microstructural data from crystal-plastically deformed zircon grains from common lithologies, where zircon

SED
6, 1799–1861, 2014

grain-sizes most commonly range from 10 to 50 micron in length. As this is the most abundant size of zircon grains in natural rocks, the data and resulting systematics are expected to be representative for the majority of zircons from various geological environments. All presented analyses were derived from thin sections of rock samples, allowing microstructural interpretations in host mineral context. The crystallographic orientation of mineral grains or grain domains was analyzed by electron backscatter diffraction (EBSD). This technique provides data at sub-micron scale spatial resolution and allows in-situ examination of a few to tens of microns sized grains.

1.3 Crystal-plastic deformation

A single crystal exposed to shear stresses deforms elastically at the initial deformation stage, but if the applied shear stresses exceed the elastic limit, geometrically necessary dislocations (GNDs) are generated in the lattice in order to accommodate the strain (Nye, 1953; Wheeler et al., 2008; Dahlberg et al., 2014); or the crystal breaks after the yield strength has been overcome (Ranalli, 1995). Crystal-plastic- or ductile deformation of individual crystals is assumed to be a consequence of formation and motion of dislocations (lattice line-defects) caused by differential stress (Poirier, 1985; Timms et al., 2011). Migration of dislocations by climb is a thermally activated process; migration by glide is a stress-induced process; at tectonic conditions that allow dislocations to move through the crystal lattice, the crystal deforms plastically by slip along a densely packed crystallographic plane. Slip direction [uvw] and slip plane (hkl) are described by Miller indices and define a slip system [uvw](hkl) (Poirier, 1985). By migration the dislocations accumulate within so-called “dislocation walls” or “subgrain boundaries” or “low-angle boundaries” (e.g. Poirier, 1985; Reddy et al., 2007). Arrays of edge dislocations with the same Burgers vector form tilt walls, whereas arrays of screw dislocations form twist walls. Tilt and twist walls are complementary, having Burgers vectors perpendicular and parallel to the respective dislocation line correspondingly (Poirier, 1985). If the misorientation axis of the active slip system is lying in the subgrain boundary, then it is assumed to be a tilt boundary. At these given conditions, the

SED
6, 1799–1861, 2014

glide direction should be normal to the tilt boundary, and the glide plane should contain both the glide direction and the misorientation axis. Opposite to this, if the misorientation axis is normal to the subgrain boundary, then it is assumed to be a twist boundary and a glide plane at the same time (Poirier, 1985; Reddy et al., 2007). All symmetrically equivalent crystallographic directions and planes which are orthogonal may represent valid glide systems (Roters et al., 2010). For example, for zircon that has tetragonal symmetry, considering two equivalent directions [100] and [010], two relevant orthogonal active glide systems are [100](010) and [010](100) (Reddy et al., 2007; Leroux et al., 1999). These two relevant glide systems could be labeled as one slip system family ⟨100⟩{010}.

1.4 Used terminology

In this study dislocation walls or subgrain (low-angle) boundaries are assumed to be intragranular microstructural planar elements that separate subgrains. Subgrains are intragranular lattice domains with no internal misorientation, but their crystallographic orientations somewhat differ, reaching relative misorientation angles from 1° to 10° between adjacent lattice domains (Ranalli, 1995). Whenever relative misorientation exceeds 10° the lattice units are identified as new grains separated by grain (high-angle) boundaries. In addition, the crystallographic orientations of subgrains are supposed to have continuous and systematic rotational trends in the pole figure. If the crystallographic axes of each domain represent a separate cluster, the boundaries between these crystal domains are regarded as high-angle boundaries or even brittle cracks. The (sub)grain boundaries are visible in 2-D sections as lines, and their traces are characterized by 200–500 nm wide linear features displayed as low-contrast EBSD pattern data points in the image quality map.

SED
6, 1799–1861, 2014

1.5 Motivation and challenge

This study contributes to basic issues of crystal-plastic deformation mechanisms in zircon. Based on microstructural observations of deformed zircon grains in association with the rock matrix of meta-igneous and meta-sedimentary rocks the following questions were addressed: is crystal-plastic deformation of zircon related to metamorphic recrystallization? Is there a similarity in zircon rheology in various rock types and at differing metamorphic grade? How do the specific shape and internal heterogeneities of a zircon grain influence its deformation behavior? Which misorientation axes and active slip systems are most common in deforming zircon grains? Does the orientation of the zircon lattice with respect to the external stress field influence the crystal-plastic deformation pattern? Does zircon develop a preferred crystallographic orientation? How does the nature and microstructure of the local environment (surrounding host phases and adjacent matrix phases) affect the finite deformation pattern of zircon? Which parameters define whether deformed zircon develops a low-angle boundary network or not?

Based on our observations we have classified the finite deformation patterns of crystal-plastically deformed zircons and discussed possible agents that define the variety of distortion patterns.

2 Geological environment

Samples were collected from shear zones in two study areas:

2.1 Western Tauern Window, Eastern Alps (Zillertal, Tyrol, Austria)

In the Tauern Window (Eastern Alps), continental and oceanic rocks of the Penninic and sub-Penninic nappe sequences are exposed, which represent the footwall of the Austroalpine nappe stack. Nappe stacking and predominant final metamorphism are related to the closure of the Alpine Neotethys and subsequent continental collision in

SED
6, 1799–1861, 2014

late Cretaceous-Tertiary (Miller et al., 2007). Samples for the present research were collected from the "Zillertaler Kern" lobe of the "Zentralgneis" formation (see Selverstone et al., 1991 and reference therein).

The magmatic protholiths of the "Zentralgneis" formation are uppermost Devonian to lower Permian in age. Three magmatic "pulses" of potassium-rich and calc-alkaline granites, felsic and intermediate volcanites and tonalitic/granodioritic plutonites can be distinguished (Veselá et al., 2011). The granitoids intruded into pre-Carboniferous, partly poly-metamorphic basement rocks consisting of various schists, para- and orthogneisses, amphibolites and meta-ophiolites. In the Zillertal section Variscan amphibolite facies regional metamorphism has been overprinted at greenschist- to amphibolite-facies metamorphic conditions of 0.5–0.7 GPa and 550–600 °C at ca. 30 Ma (Selverstone, 1985; Pennacchioni and Mancktelow, 2007). Metamorphic (re)crystallization was accompanied by the formation of ductile extensional shear zones (Pennacchioni and Mancktelow, 2007). The sampled shear zones No. 1 and 2 (see description below) presumably formed during this latter tectono-metamorphic event.

2.2 Ivrea-Verbano Zone, Southern Alps (Forno, Val Strona, Northern Italy)

The Ivrea-Verbano Zone (IVZ) consists of a NE–SW trending, steeply dipping sequence of meta-sedimentary and meta-igneous basic rocks, ultrabasic mantle tectonites and a large underplated igneous complex. The sequence consists of predominant metasedimentary rocks in the SE and prevailing metabasic rocks and strongly depleted metapelites in the NW. Metamorphism increases progressively from amphibolite facies in the SE to granulite facies in the NW. The Ivrea-Verbano Zone is supposed to represent a section through the lower continental crust that experienced regional metamorphism during the uppermost Palaeozoic (Rutter et al., 2007; Quick et al., 2009).

Within the Ivrea-Verbano Zone a network of high-temperature shear zones, which are subparallel to the NE–SW elongation direction of the IVZ are observed. The shear zone network extends from Anzola (Val d'Ossola) to Forno (Val Strona) and can be traced for more than 20 km in length (Brodie et al., 1992). Single shear zones range in

SED
6, 1799–1861, 2014

width from a few centimeters to more than 10 m, and are rarely as much as 200 m thick. Mylonites in the northern part of the Ivrea-Verbano zone completely (re-)equilibrated under granulite-facies conditions prevailing during crustal attenuation/extension and contemporaneous magmatic underplating (Rutter et al., 2007) between 315 Ma and 270 Ma (Rutter et al., 2007, Quick et al., 2009, Sinigoi et al., 2011). In the Val Domodossola section at Cuzzago peak P-T estimates are 0.6–1.0 GPa and > 800 °C, based on the peak P-T estimates from the neighboring Val Strona di Omegna (Redler et al., 2012).

3 Sampling localities

3.1 Western Tauern Window, Zillertal, Tyrol, Austria, east of Berliner Hütte

3.1.1 *Shear zone 1* (47°01′39.308″ N latitude, 11°50′3.669″ E longitude to 47°01′39.987″ N latitude, 11°50′6.311″ E longitude)

The ~50 m thick ductile shear zone is exposed on the NE slope of the Zemmbach side valley (Sturm and Steyrer, 2003). The shear zone represents strongly foliated quartz-biotite orthogneiss containing mylonitic layers that are leucocratic and depleted in mafic minerals compared to the gneiss. The highly foliated gneiss is enriched in biotite and white mica (Fig. 1a). The host rock of granitic composition is weakly foliated and crosscut by leucocratic veins.

3.1.2 *Shear zone 2* (47°01′18.129″ N latitude, 11°50′26.709″ E longitude)

A strongly foliated quartz-biotite orthogneiss hosts two adjacent deformed dykes, a leucocratic aplitic dyke and a melanocratic, presumably metalamprophyric dyke (Fig. 1b). The leucocratic dyke shows thickness variations from 20 cm to 1.5 m and locally presents a cuspate-lobate structure along the lithological contact 1 (Fig. 1b, arrow). Within aplitic dyke at hand specimen scale garnets, large green K-feldspar clasts,

SED
6, 1799–1861, 2014

quartz veins and mica-rich thin layers are distinguishable. On the lower contact (contact 2, Fig. 1b) with the leucocratic dyke, gneiss is intruded by the mafic dyke. Mafic dyke is extremely foliated and folded and apparently accommodate the highest strain intensity representing the rheologically weakest lithology in the sequence. Quartz-biotite gneiss in contact with the mafic dyke (contact 3, Fig. 1b) is also highly foliated. The high-strain zone in gneiss adjacent to contact 3 is about 1 m thick, whereas next to the contact 1 with the aplitic dyke, the gneiss is less foliated and the sheared zone is narrower (∼10 cm).

3.2 Ivrea-Verbano Zone, Northern Italy, vicinity of the village Cuzzago

Shear zone 3 (45°59′45.64″ N latitude, 8°21′38.75″ E longitude): the sampling locality near the village of Cuzzago (Val d'Ossola) shows non-foliated metasedimetary granulite-facies rocks, locally known as stronalites. Stronalites are crosscut by discordant layer of sillimanite-biotite-garnet gneiss that is considered to be a restitic material from partial melting of metapelite (Barboza et al., 1999). Sample material was taken from a several meters thick non-folilated metasediments (Fig. 1c). At the outcrop scale this rock locally has a compositional layering, which is folded.

4 Petrography and zircon content

The accessory minerals in lithological descriptions are listed in order from least to most abundant. Microstructural data of zircons from the Tauern Window are shown in Figs. 2–9 and 13, from the Ivrea-Verbano zone in Figs. 10–13.

4.1 Shear Zone 1

Sample BH12-01-II was collected from an ultramylonitic layer that represents the core of the shear zone and has a sharp contact with the host gneiss even at thin section scale. The ultramylonitic layer is composed of a fine grained, recrystallized plagioclase-

SED
6, 1799–1861, 2014

quartz matrix (grain size: 70–300 µm in diameter, > 95 vol. % of the layer), with minor modal content of biotite, white mica and epidote (<5 % in total), which form a weak foliation. Along plagioclase phase boundaries a few microns-thin K-feldspar-veins occur. Zircon, apatite, and titanite are common accessory minerals. Zircon forms small (5–10 µm in diameter) rectangular grains, with aspect ratios from 1 : 1 to 1 : 3. The zircon crystals are characterized by a dark CL-signal in the core and a bright thin outer rim (Fig. 6b), where core has relatively low degree of crystallinity, according to Raman spectroscopy. Two grains from this zone have been analyzed by EBSD, wherefrom one grain exhibits finite crystal-plastic deformation.

The gneiss from shear zone 1 contains plagioclase, quartz, a large amount of biotite and white mica, as well as K-feldspar veinlets. Biotite is locally replaced by association of titanite, chlorite, quartz and epidote. The even or sigmoidal foliation is represented by leucocratic layers of plagioclase-quartz and layers consisting of plagioclase, quartz, biotite, white mica and epidote. In some domains the foliation is defined by pure mica bands. Zircons in this sequence have 2 to 50 µm grain size and are hosted by plagioclase or biotite grains, sometimes associated with epidote and apatite. The smaller non-deformed grains show oscillatory and sector zoning which is truncated by recrystallization zones or marginal overgrowths, which both appear bright in CL-images (Fig. 2b). The largest grains are cracked and dispersed in the matrix (Fig. 8).

Samples *BH12-01-I* and BH12-02–04 are granitic gneisses with varying degrees of deformation. Sample *BH12-01-I* was taken adjacent to ultramylonitic highly-foliated biotite gneiss. 57 % of the investigated zircon grains show evidence of crystal-plastic and/or brittle deformation. Sample BH12-02 exhibits lower deformation intensity than the BH12-01 series, and contains about 46 % of deformed zircon grains. Sigmoidal clasts of plagioclase and quartz in the mylonitic gneiss of sample BH12-02 show top to WSW sense of shear. Samples BH12-03 and BH12-04, collected from the host rock of shear zone 1, are weakly deformed, non-foliated or weakly-foliated granitic orthogneisses. They contain around 16 % crystal-plastically and/or brittlely deformed

SED
6, 1799–1861, 2014

zircon grains. A schematic histogram of shear zone 1 with content of deformed zircon grains is shown in Fig. 14a.

Data on zircons from shear zone 1 are presented in Figs. 2, 6–8 and 13.

4.2 Shear Zone 2

Sample BH12-05 has no clear foliation and contains large, up to 1 cm sized irregular-shaped clusters of biotite grains without shape preferred orientation. The sample contains several, variably oriented small-scale paired shear zones (Pennacchioni and Mancktelow, 2007) adjacent to epidote veins. Samples BH12-05–06 are biotite gneisses, compositionally close to samples BH12-01–04. Sample BH12-06-I is a strongly foliated gneiss whereas BH12-06-II represents a biotite gneiss with sigmoidal foliation. Zircon grain size in these lithologies varies from 10 to 100 µm, with most grains having euhedral shape and oscillatory and sector zoning (Fig. 3b). Some of them represent the fragments of larger preexisting grains. About half of the zircon grains (40 to 60 %) in different parts of the gneiss sequence were crystal-plastically and/or brittlely deformed.

Sample BH12-07 was collected from a mafic dyke. As the rheologically weakest lithology in the overall inhomogeneous sequence, the mafic dyke accommodated the highest strain. The sample is chlorite-rich (>50 % modal content) due to intense retrogression of biotite. The sample is composed of mafic layers consisting of chlorite, biotite and titanite, with an average thickness of 1–6 mm. Mafic layers alternate with fine grained plagioclase-quartz layers of the same thickness range. The compositional layering is isoclinally folded. The accessory minerals are calcite, pyrite, zircon, rutile and titanite. Zircon is present as small (10–30 µm) euhedral grains with degraded CL-zonation. Small xenocrystic cores and oscillatory-zoned rims are sometimes distinguishable in the CL images (Fig. 5b). 53 % of all analyzed zircon grains indicate crystal-plastic or brittle deformation.

SED
6, 1799–1861, 2014

Sample BH12-08 is taken from the aplitic dyke. The rock is almost non-foliated and contains only a small fraction of crystal-plastically deformed zircon grains (8 %), none of those are presented in this paper.

Schematic histogram of shear zone 2 with content of deformed zircon grains is shown in Fig. 14b. Data on zircons from the shear zone 2 are presented in Figs. 3–5, 9 and 13.

Within the sequences of shear zones 1 and 2, the initial amphibolite-facies paragenesis is locally replaced by mineral phases that are characteristic for greenschist-facies metamorphic conditions. The association of plagioclase + quartz + biotite is ubiquitously decomposed to K-feldspar + albite + epidote + Al-titanite ± calcite ± rutile. Local chlorite-pseudomorphs after biotite supposedly represent a retrograde greenschist-facies stage of metamorphism. K-feldspar-, calcite- and epidote-rich veins as well as some dissolved zircon surfaces and healed cracks decorated by inclusion trails, are evidence of intense fluid infiltration.

4.3 Shear Zone 3

Sample IV12-06C is representative of shear zone 3 from the Ivrea-Verbano zone. It is a massive rock, consisting of large garnet grains (0.5–5 mm in diameter) that are cracked and have an irregular shape. Locally garnet forms aggregates of smaller grains sized from 40 to 80 µm that form a foliation pattern. The space between the garnet clasts is filled with Mg-rich biotite (phlogopite), quartz and plagioclase. These phases occur in two grain sizes: 100–250 µm and below 10 µm. Plagioclase and biotite sometimes form thin symplectitic intergrowths. The zircons range from 20 to 50 µm in diameter and mostly have a roundish shape. Zircon grains form inclusions within garnet but more often occur in the plagioclase-quartz matrix. In CL images they contain a dark core and a thick bright homogeneous rim (Fig. 10b). Around 11 % of grains, investigated for orientation contrast, appeared crystal-plastically deformed, and 24 % appeared to be deformed brilltely. Only irregularly-shaped grains display crystal-plastic deformation (Figs. 10 and 12), and they are found in the domains with large-grained garnet.

SED
6, 1799–1861, 2014

Data on zircons from the shear zone 3 are presented in Figs. 10–13.

5 Analytical methods and data representation

5.1 Sample preparation

Zircons were examined in-situ using polished thin sections, mechanically prepared with 0.25 µm diamond paste and subsequently chemically polished with alkaline colloidal silica solution (Köstrosol 3530; pH 9.2–10) on an active rotary head polishing machine for 4 h. Samples were cleaned in ethanol and distilled water before carbon coating (2 carbon-threads for SEM- BSE and CL imaging, 1 carbon thread for FSE and EBSD analysis) to establish electrical conductivity.

5.2 Scanning electron microscopy and cathodoluminescence (CL) imaging

All zircons were identified and characterized by backscattered-electron (BSE) and cathodoluminescence (CL) imaging in order to identify the internal microstructures, select areas for FSE imaging, EBSD and Raman analysis and to investigate the host mineral phases, using an FEI Inspect S scanning electron microscope equipped with a Gatan MonoCL system. Imaging conditions were at 10 kV accelerating voltage, CL-image resolution of 1500 × 1500 to 2500 × 2500 pixels using a dwell time of 80.0–150.0 ms and probe current/spot size 4.5–5.0.

5.3 Electron backscatter diffraction (EBSD) analysis and forescattered electron (FSE) imaging

Zircon grains were examined for potential crystal-plastic deformation structures using orientation contrast images (Reddy et al., 2007). These were taken using a forescattered-electron detector (FSD) mounted on the EBSD-tube of an FEI Quanta 3-D FEG instrument (Center of Earth Sciences, University of Vienna, Austria), which

SED
6, 1799–1861, 2014

is equipped with a Schottky field emission electron source. During FSE imaging the tube was retracted by about 5 mm from the completely inserted position in order to obtain maximum FSE signal intensity. Electron beam conditions were 15 kV accelerating voltage, 2.5–4 nA probe current using the analytic (high beam current) mode. Forescattered electron detector settings were close to maximum gain both for the detector voltage and signal amplification. Stage settings were at 70° tilt and 14–16 mm working distance. After identification of the potentially deformed grains, EBSD orientation mapping was applied to selected zircon grains. The FEI Quanta 3-D FEG instrument is equipped with an EDAX Pegasus Apex 4 system consisting of a Digiview IV EBSD camera and an Apollo XV silicon drift detector for EDX analysis. EDX intensities and EBSD data were collected contemporaneously using the OIM data collection software v6.21. Stage and beam settings for EBSD analysis were the same as for FSE imaging, but the EBSD camera was completely inserted during EBSD data collection. An EBSD camera binning of 4 × 4 was used at exposure times of 50–130 ms. In addition to a background subtraction filter, a histogram normalization filter as well as a dynamic background subtraction filter was applied to enhance EBSD pattern contrast. As zircon yielded a significantly higher EBSD signal intensity than the matrix phases (used for background calibration), the EBSD camera exposure time was significantly reduced after background collection in order to avoid signal oversaturation during zircon analysis. Therefore, the matrix phases collected at these settings yielded very weak pattern contrast. Hough parameters were set to a binned pattern size of 9 × 9 pixels, a Theta step size of 1° and a Rho-fraction of 74–86 %. After applying a 9 × 9 convolution mask 3–15 bands with a minimum pattern contrast of 200 and at a minimum peak distance of 3–10 pixels in Hough space were used for indexing. At the given settings indexing rates were between 6 and 24 points per second. Orientation maps were obtained from beam scanning in hexagonal grid mode at step sizes of 0.1–0.16 µm.

The EBSD data are represented in the sample reference frame and presented in two mapping modes. The first mapping mode is false color-coded misorientation maps, with colors showing the relative angular misorientation of each data point with respect

SED
6, 1799–1861, 2014

to a user-selected single reference point within the grain (indicated by a red marker); the second mode is local misorientation maps, where each pixel is colored according to the mean misorientation of the respective data point relative to the neighboring points. The orientations of the crystallographic axes are plotted as lower hemisphere equal area projections and are color-coded according to the corresponding EBSD map of the first mapping mode. The first mode of maps and pole figures were produced using the EDAX OIM Analysis software v6.2.1, whereas the second mode of misorientation maps (local misorientation maps) were generated with the MTEX toolbox for MATLAB (Bachmann et al., 2010, 2011; Mainprice et al., 2011).

Every misorientation between two crystal lattices (also termed "disorientation" in the literature, e.g. Reddy et al., 2007) can be characterized by two parameters, the rotation angle and rotation axis which allows to rotate one lattice into the orientation of the other. We used MTEX toolbox for plotting histograms of misorientation angles between datapoints as well as for visualizing the misorientation axis orientation and density contours in inverse pole figures.

5.4 Raman spectroscopy

Raman spectra were acquired on a confocal edge filter-based Renishaw RM1000 micro-Raman system equipped with a 50 mW multimode Ar^+-laser (using the 488 nm emission at ~20 mW), a 1200 lines mm^{-1} grating, and a thermo-electrically cooled CCD detector. Raman intensities were collected with a Leica DMLM microscope with 50 ×/0.75 or 100 ×/0.90 objectives. These settings resulted in a spectral resolution of ~4 cm^{-1} and a spatial resolution of better than ~3 µm. Spectra were recorded for 30 s in the range from −50 cm^{-1} (to get also the Rayleigh line at 0 cm^{-1} for internal calibration) to 1580 cm^{-1}. Instrument control and basic data processing was done with Grams32 software (Galactic Industries Corp., 1996). Exact peak positions and peak widths (FWHM = full width at half maximum) were extracted (after shift correction according to the Rayleigh line) with the software PeakFit 4.12 (SeaSolve Software Inc., 1999–2003).

SED
6, 1799–1861, 2014

Raman analyses were used to compare the degree of crystallinity in various zircon grain domains. For this goal a color-coding scale, based on the range of degree of crystallinity of all analyzed spots was created. The data points are superimposed as colored dots on CL images.

6 Microstructural and crystallographic orientation data

The characteristic feature of zircon grains in granitic gneisses from shear zones 1 and 2 is that CL-bright domains truncate initial oscillatory zoning. CL-bright domains are often forming several mutually crosscutting generations within a single grain. *Grain 29* (Fig. 2a–c) from sample *BH12-01-I* shows semi-circular CL-bright intragranular domains with smooth or ragged domain-boundaries (Fig. 2b). They lack significant misorientation with respect to the remaining grain, showing orientation variations of less than 0.5° (Fig. 2a and d). Raman spectroscopy documented an increased degree of crystallinity of the CL-bright domains (Fig. 2b).

Crystallographic orientation maps show intragranular orientation variations within some of the zircon grains that are discussed below.

Grain BH12-05B_07 (Fig. 3) is hosted by a biotite aggregate that is decoupled from the zircon grain, as it is shown by normal and reverse drag of the adjacent biotite (Fig. 3a). Zircon grain has an elongated idiomorphic, almost elliptical shape and performs lattice distortion on its upper left portion, reaching a maximum intragranular misorientation of about 3°. The subgrain boundary appears in the CL image (Fig. 3b) as a thin bright linear feature truncating the oscillatory zoning, and also forms curved traces in the EBSD map (Fig. 3a and c). The misorientation axes are arranged along a great circle in the inverse pole figure plot (dashed line in Fig. 3d). The curved trace of a subgrain boundary (Fig. 3a–c) and the distribution of misorientation axes along the great circle (dashed line in Fig. 3d) are the features of cross slip (Poirier, 1985; Reddy et al., 2007), which in this case results from the activity of different slip planes, e.g. Zrn (332), (321), (510) and (100) (Fig. 3d).

SED
6, 1799–1861, 2014

Grain BH12-07B_28 (Fig. 4) is hosted by biotite and has a prismatic euhedral shape (Fig. 4c). Zircon grain is decoupled from the host biotite, what could be concluded from normal and reverse drag of the surrounding biotite (Fig. 4c). Grain shows maximum intragranular orientation variations of 6° (Fig. 4a and e). The subgrain boundaries stretch from lower left to upper right (Fig. 4a–c, and e), and their traces extend in C' geometry with respect to the mylonitic foliation. Subgrain boundaries appear bright in the CL image (Fig. 4b, white arrows). The degree of crystallinity does not vary significantly across the grain (Fig. 4b). Crystallographic orientation data of zircon show a clear concentration of the misorientation axes around the Zrn [001] (c-axis), consistent with the crystal axes rotation along small circles around the undispersed cluster of Zrn [001] (Fig. 4d and f).

Grain BH12-07B_15a (Fig. 5) from the same sample is also surrounded by biotite and has rectangular short-prismatic shape. The EBSD map shows an intragranular orientation variation of 5°. The grain contains a network of approximately orthogonal subgrain boundaries (Fig. 5a–d). These separate distinct subgrains with clear orientation contrast (Fig. 5d) and appear bright in the CL image (Fig. 5b, white arrows). Within the grain a CL-bright xenocrystic core is observed. Some subgrain boundaries intersect this core domain; others terminate at its boundary (Fig. 5b, c, upper part of the grain). Concentric growth zones show an increasing degree of crystallinity towards the rim (Fig. 5b). The misorientation axes inferred from misorientations of the subgrains are parallel to Zrn [001] and [100] (Fig. 5e) whereas the crystal axes do not show a clear rotation trend (Fig. 5f).

Grain BH12-01B_22 (Fig. 6), from the ultramylonite core of shear zone 1, is located in plagioclase, has elongated euhedral shape and displays subgrain boundaries emanating from mineral inclusion (Fig. 6a). Subtle cracks in the host plagioclase (Fig. 6c, black arrows) intersect the zircon phase boundary at the positions close to those of the zircon subgrain boundary-intersects. The CL image reveals not only a dark core and a bright outer rim, but also a linear CL-bright zone that is spatially associated with a subgrain boundary (Fig. 6b, white arrows).

SED
6, 1799–1861, 2014

Scan BH12-04_11 (Fig. 7) covers two idiomorphic zircon grains that are hosted by polycrystalline plagioclase (Fig. 7d). One of the Zrn grains has elongated shape with aspect ratio 1 : 5 in the 2-D section, whereas another is rather isometric. The elongated grain shows grain-internal orientation variations of about 5° due to the presence of subgrains, which show strong orientation contrast although subgrain boundaries do not appear in the CL image (Fig. 7a, b and d). Within the subgrains orientation variations are negligible. The grain boundary trace of fine-grained plagioclase at the left (Fig. 7a and d, white arrow) is oriented at a high angle to the trace of the zircon prismatic face. The coarser plagioclase grain covering the upper left of the map shows grain-internal orientation contrast, and a plagioclase subgrain boundary trace oblique to the zircon prismatic face (Fig. 7d, black arrow, dashed line). The plagioclase (sub)grain boundaries impinge on the zircon phase boundary at the same sites as the subgrain boundaries within the zircon. The misorientation axes show a maximum parallel to Zrn [320] (Fig. 7e).

Domain BH12-02_45 (Fig. 8) represents a zircon aggregate hosted by plagioclase and quartz and consists of differently oriented irregularly-shaped fragments. Some fragments seem detached from the aggregate and surrounded by host plagioclase in the 2-D section (Fig. 8c, upper right, lower left). Zrn-fragments are separated by low- and high-angle boundaries, and the misorientation angles between fragments range from 2° to more than 15° (Fig. 8c). Grain boundaries characterized by a CL-bright signal truncate oscillatory zoning (Fig. 8b). The distribution of misorientation axes does not show systematics of fragments rotation (Fig. 8e), consistent with unsystematic scattering of Zrn crystallographic orientations (Fig. 8f).

Grain BH12-07A_03a (Fig. 9a) is situated at the phase boundary between polycrystalline chlorite and potassium feldspar, whereas *grains BH12-07A_04* and *BH12-07B_31b* occur within biotite aggregates (Fig. 9b and c). Grain BH12-07A_03a shows decoupling from the matrix. All three grains have sub-idiomorphic shape, are elongated with aspect ratios 2 : 3–1 : 2 and display subgrains with 4°–10° orientation deviation from a reference point. Grains show systematic lattice rotation about Zrn [001] (right

SED
6, 1799–1861, 2014

column). According to the subgrain boundary configurations active slip system in these grains is ⟨100⟩{010}. The [001] directions of all three grains have a similar orientation (highlighted by a red circle) coinciding with that of crystal BH12-07B_28 (Fig. 4f).

Domain IV12-06C_05 is situated at the phase boundary between a polycrystalline plagioclase aggregate and a single garnet grain (Fig. 10e). The zircon aggregate has irregular shape with curved boundaries and shows significantly higher intragranular orientation variations than all previously presented samples reaching 35° (Fig. 10a). However, the misorientation is almost indistinct in the FSE orientation contrast image (Fig. 10e). Subgrain boundaries occur locally, terminating within the grain, and are coupled with a gradual bending of the rim (Fig. 13b). A few grain boundaries are presented (Fig. 10d, green and blue contours), indicating formation of the new zircon grains next to the garnet-zircon boundary. The CL image (Fig. 10b) yields a dark core and bright rim. The degree of crystallinity gradually decreases towards the deformed part of the grain (Fig. 10b). The pole figure shows a complex rotation pattern of the crystallographic axes. The rotation trend splits into two major parts (Fig. 10f, black arrows). Consistently, the misorientation density distribution plot shows two density peaks for misorientation axes that are at a mutual angle of about 45° clustering around [331] and close to [100] (Fig. 11a).

Grain IV12-06C_16 is hosted by a polycrystalline plagioclase aggregate. The grain is elongated normal to its c-axis and has an anhedral shape with a smoothly curved boundary trace (Fig. 12). It shows a high grain-internal deformation that amounts to 25° intragranular orientation variation, but forms no (sub)grain boundaries (Fig. 12a and c). The orientation gradually changes by about 0.6° to 1.4° per µm (Fig. 13a), so that the misorientation between single points within the grain does not reveal any distinguishable features (Fig. 12c). The orientation contrast image displays an undulatory pattern (Fig. 12d). The CL image has a uniformly bright signal without strong zoning or mantle-core structure, and the degree of crystallinity does not change significantly across the crystal (Fig. 12b). Misorientation data demonstrate a scattered distribution

SED
6, 1799–1861, 2014

of the misorientation axis with a higher density close to Zrn [001], however, the pole figure shows clear lattice rotation around Zrn [001] (Fig. 12e and f).

7 Microstructural analysis and interpretation

7.1 Static hydrothermal recrystallization vs. crystal-plastic deformation

Hydrothermally altered zircon zones resembling those in grain BH12-01B_29 (Fig. 2), have been described from natural rocks (e.g. Corfu et al., 2003) and produced experimentally (Geisler et al., 2001, 2003). Altered zones that crosscut the initial zoning are characterized by a sharp front with curved geometry separating altered from pristine zones within the grains. Recrystallized lattice domains are marked by increased CL intensity compared to the signal from the matrix, which is considered to be a result of dissolution-precipitation recrystallization and decreased lattice defect density due to recovery (Corfu et al., 2003; Geisler et al., 2001, 2003). There are at least four arrangements of CL-bright domains observed in investigated zircons: (i) CL-bright domains extend into the inner parts of a grain, forming closed core zones (e.g. Fig. 2b, upper left part, lower right part); (ii) they are observed along cracks or subgrain boundaries (Fig. 6b); (iii) they occur as rims, framing the central part of a crystal (Fig. 10b), or (iv) cover the entire grain (Fig. 12b).

i Zircon grain BH12-01B_29 (Fig. 2, sample *BH12-01-I*) does not show a genetic relation of CL-bright homogeneous domains and crystal-plastic deformation. Recrystallized domains do not exhibit any significant misorientation with respect to the rest of the grain (Fig. 2d). Slight misorientation corresponding to intensity variations in the CL pattern can be interpreted as related with a compositional variation and the increased degree of crystallinity (Fig. 2a and b). Homogeneous CL-bright domains (i) forming closed zones with half-circular shape inside the crystal, frequently occur in sample *BH12-01-I*. Their occurrence is independent of whether grains show crystal-plastic deformation microstructures or not, leading to

SED
6, 1799–1861, 2014

the conclusion that crystal-plastic deformation and recrystallization in this sample have no evident mutual effect.

ii In contrast, grain BH12-01B_22 (sample BH12-01-II) demonstrates a genetic relation between recrystallized zones and crystal-plastic deformation microstructures. The CL-bright feature left of the inclusion is also visible in the SE image (Fig. 6c, white arrows) and spatially corresponds with the trace of the subgrain boundary that accumulates the largest misorientation angle (Fig. 6b, white arrows; d, boundary color-coded green). However, the significant width of this CL bright zone contrasts with similar features observed in grains *BH12-05B_07*, BH12-07B_15a and 28. The geometric relationship between CL-signal characteristics and subgrain boundaries indicates that hydrothermal recrystallization postdated crystal-plastic deformation and exploited deformation microstructures. Subtle cracks in the hosting plagioclase (Fig. 6c, black arrows) are spatially associated with the crystal-plastically-deformed part of the zircon grain and might be related to the slight volume expansion of the zircon grain's tip due to recrystallization and/or, more likely, metamictization of the CL-dark core.

iii In grain IV12-06C_05 (Figs. 10 and 11) the CL-bright recrystallized rim (iii) is locally deformed and exposed to the local grain size reduction. The degree of crystallinity is rather low where lattice distortion took place. The local distortion of the recrystallized rim shows that metamorphic recrystallization of zircon predates plastic deformation. The thickness of the recrystallized rim is reduced in the crystal-plastically-deformed zone when comparing with the average thickness of the undistorted rim in the lower portion of the grain. The bright rim almost disappears where newly formed grains are observed (Fig. 10b and d – domains with green and blue contours).

iv Grain IV12-06C_16 is homogeneously bright in the CL image (Fig. 12b), potentially reflecting complete recrystallization. Homogenization of the crystal lattice and chemical composition – if predating deformation – could explain the lack of

SED
6, 1799–1861, 2014

strain localization and subgrain formation in this Zrn grain. Another possibility is that the bright CL-signal is generated by dislocations, which represent evenly distributed luminescence centers in the crystal lattice. The bright CL-signal induced by intrinsic defects in the crystal lattice including dislocations has been described for calcite, quartz, and some synthetic materials (e.g. Goetze et al., 2001; Akchurin et al., 2009).

To summarize, zircon recrystallization in the investigated samples supposedly was induced by fluid infiltration. Where observed, the temporal relationship between hydrothermal recrystallization and crystal-plastic deformation may vary: in one sample hydrothermal alteration clearly precedes crystal-plastic deformation (IV12-06C_05), in the other postdates (BH12-01B_22), whereas sometimes the relative timing is not clear (IV12-06C_16). Hydrothermal alteration causing dissolution-precipitation may have been operating repeatedly at different stages and in different temperature regimes during the metamorphic evolution of the rocks.

7.2 Zircon lattice distortion types

Three main types of zircon lattice distortion patterns were distinguished (see Table 1), based on the absence (type I) or presence (type II and III) of well-developed subgrain boundaries in strained zircon grains. Type II contains half-circular shaped subgrain boundary traces with high misorientation (more than 10°) whereas type III shows continuous low-angle boundary networks (less than 10° misorientation). Our classification is consistent with that suggested by Piazolo et al. (2012).

Type (I) and (II) patterns seem to be predominant in rocks that had experienced granulite-facies metamorphic conditions, whereas type (III) is more common in the amphibolite-facies rocks.

SED
6, 1799–1861, 2014

7.2.1 Distortion type I

Type (I) finite deformation patterns are characterized by gradual intragranular lattice orientation changes affecting the entire zircon grain without any remarkable step or subgrain formation. Similar features have been described by Reddy et al. (2007), and very likely correspond to type I lattice distortions of the classification by Piazolo et al. (2012). Moser et al. (2009) describe this type of lattice distortion as a result of an impact event.

Uniform bending of the zircon lattice reaching intragranular misorientations up to 25° (Fig. 13a) requires the presence and even distribution of geometrically necessary dislocations (GND), which form if the lattice rotations exceed its elastic limit. However dislocations obviously are not mobile and therefore do not accumulate within (sub)grain boundaries. Grain IV12-06C_16 (Fig. 12) shows rather high grain-internal deformation accounting for 25° misorientation with respect to a single reference point (Fig. 12a). Due to uniformly distributed dislocations the zircon lattice seems to be gradually bent equivalent to undulatory extinction, although the grain is too small to display this phenomenon in an optical light microscope. Distributed strain, accommodated by dislocations that are not accumulated in low angle boundaries does not allow inferring active slip systems although the misorientation axes are mostly parallel to Zrn [001]. The degree of crystallinity and CL-intensity does not significantly change across the grain, which is likely a result of the uniform distortion (Fig. 12b).

7.2.2 Distortion type II

This deformation pattern is grain size reduction and characterized by strong lattice distortion in local rim domains within grains. This lattice distortion preferably develops in zircon domains adjacent to a rheologically relatively strong phase as well as in grains hosted by polycrystalline fine-grained matrix. Collision with a strong neighboring grain leads to differential stress and eventually to strain in specific grain domains. The upper left part of the zircon grain IV12-06C_05 collided with the adjacent garnet grain (Fig. 10)

SED
6, 1799–1861, 2014

resulting in high lattice strain with relatively large angular misorientations of more than 35° with respect to a reference point (Fig. 10a).

Unlike the lattice distortion type (I), type (II) demonstrates (sub)grain boundary formation developed within distorted zircon rims. (Sub)grain boundaries have a half-circular open shape with the convex side facing towards the undistorted grain domains (Fig. 10d). They often terminate inside the grain. The point-to-origin misorientation profile of deformed grains shows gradual distortion and sharp steps when crossing the subgrain boundaries (Fig. 13b). The degree of crystallinity is decreased in the strained domain with respect to the rest of the grain (Fig. 10b, colored dots) consistent with an increase of local misorientation angles.

Finite deformation pattern type (II) includes not only subgrain formation, but also the formation of high-angle grain boundaries and grain size reduction. Dynamic recrystallization by a subgrain rotation mechanism initially causes the formation of low-angle boundaries, whereas progressive strain accumulation induces further subgrain rotation and an increasing dislocation density in the subgrain boundaries that develop to the high-angle boundaries. Newly formed grains are observed in the Fig. 10d, contoured by blue lines.

The crystallographic orientations in the pole figure show asterism (Fig. 10f), which points to several simultaneously operating slip systems with different misorientation axes. Lattice rotation along a profile normal to the zircon/garnet boundary yields misorientation axes clustered around Zrn [331], whereas a misorientation profile parallel to the phase boundary yields a misorientation axis around the Zrn [100] (Fig. 11b and c). This is consistent with the misorientation axes distribution density plot that demonstrates two clusters correspondingly (Fig. 11a). These are the main misorientation axes observed, but there could be several subordinate axes operating simultaneously (Fig. 11a).

SED
6, 1799–1861, 2014

7.2.3 Distortion type III

Type (III) is characterized by "polygonization" (Ranalli, 1995), due to formation of slightly misoriented subgrains which lack internal lattice strain, separated by subgrain boundaries. Subgrain boundaries form closed contours and often have a bright CL-signature (e.g. Figs. 3–5). The subgrains are clearly visible in the orientation contrast images. Misorientation profiles show sharp peaks for point-to-point misorientation and steps for misorientation with respect to a single reference point when crossing traces of subgrain boundaries (Fig. 13c). The type (III) distortion pattern presumably results from mechanisms such as formation and migration of dislocations, thermally-controlled recovery and recrystallization by rotation of subgrains. These are the components of dislocation creep regime and lead to accumulation of dislocations within subgrain boundaries (Poirier, 1985).

The type (III) finite deformation pattern can be subdivided into five groups, according to the dominant factors controlling the crystal-plastic behavior of zircon:

Group III-1 is defined by favorable shape orientation of deformed grain in the local stress field. These zircon finite deformation patterns that develop only locally; distortion, for example, affects the portion of grain comprising the intersection of prism and pyramid faces in euhedral prismatic zircon grains (or similar geometry, e.g. Figs. 3 and 9b; Moser et al., 2011). For this lattice distortion pattern to form, elongated elliptical or roundish inclusion, which is decoupled with the matrix, is required. The observed local deformation of the grain (Figs. 3c and 9b) implies the presence of differential stress and, therefore, inhomogeneous strain distribution within the grain. This scenario can occur in case of strong, highly viscous, elliptical inclusions in a less viscous matrix affected by simple shear, and only in case when inclusion is decoupled with the matrix (Kenkmann, 2000; Shcmid and Podladchikov, 2005). The highest pressure affects those portions of matrix, which are adjacent to the clast boundary segments normal to the shortening direction (e.g. Schmid and Podladchikov, 2004; Manktelow, 2008). According with numerical modeling (Schmid and Podladchikov, 2005) portions of the clast

SED
6, 1799–1861, 2014

adjacent to those boundary segments are exposed to relatively higher pressure, and, therefore, cause differential stress inside the grain. However, the strain rates within the adjacent soft matrix should be still much higher than within the rigid grain, so the matrix accommodates most of the strain. That is why the resulting intragranular misorientation of zircons from this lattice distortion group is usually subtle and does not exceed 5°. Other portions of grain, which are not affected by differential stress, remain undistorted.

This finite deformation pattern can be observed in *grain BH12-05B_07* (Fig. 3). The elongated, nearly elliptical zircon grain is hosted by rheologically weaker biotite aggregate; and its portion adjacent to pyramid-prism conjugation is deformed. Presumably distortion in this domain formed due to differential stress, and, therefore, inhomogeneous strain distribution during shearing; and was defined by decoupling from the matrix.

Another example of this lattice distortion type is grain BH12-07A_04 (Fig. 9b). An elliptical inclusion, enclosed in biotite and decoupled from host, is deformed at the opposite grain portions with intragranular misorientation of about 4°. From the distribution of distorted domains that are assumed to be corresponding with domains affected by differential stress during shearing, one can reconstruct the shortening direction.

It does not matter what slip systems and crystal-plastic deformation mechanism are active for the lattice distortion type (III)-1. The presence of local lattice distortion due to shape preferred orientation and decoupling with the matrix is significant. Thus, in the *grain BH12-05B_07* cross-slip is observed, and in the *grain BH12-07A_04* slip system ⟨100⟩{010} is active. The latter has not only shape favorable orientation, but crystallographic favorable orientation as well, and thus also conforms to the deformation pattern group (III)-2 (see below).

Group III-2 is defined by favorable crystallographic orientation in the local stress field. This lattice distortion patterns are controlled by the crystallographic anisotropy of zircon, causing slip along the dominant slip systems that are genetically connected with the main crystallographic axes [001], [100] and [010]. This lattice distortion group was mostly observed in the grains hosted by rheologically weaker matrix. In order to

SED
6, 1799–1861, 2014

activate dominant slip systems certain crystallographic orientation with respect to the local stress field is preferable. Grains, characterized by this deformation pattern usually perform specific shape geometry, they are rather short prismatic with the aspect ratio 1 : 2, or isometric; most of them have nearly rectangular shape (Figs. 4, 5, and 9).

There are 3 possible slip systems formed by edge dislocations, generating tilt subgrain walls: ⟨100⟩{010}, ⟨010⟩{001} and ⟨001⟩{010}. Each of those has 2 possible relevant glide systems (Leroux et al., 1999; Reddy et al., 2007, Table 1; Timms et al., 2012; Piazolo et al., 2012). Furthermore, there are also possible slip systems formed by screw dislocations, resulting in twist subgrain walls: ⟨010⟩{100} and ⟨001⟩{100} (Reddy et al., 2007). These systems we assert as "dominant", as more favorable for zircon crystals, and all the other systems, if active, "unfavorable", as less energetically-preferable.

An example of a tilt wall of a subgrain is presented in the zircon sample BH12-07B_28 (Fig. 4). Assuming that the boundary wall is parallel to (100) and the misorientation axis is oriented parallel to [001] (Fig. 4d and f), the resulting slip system is [100](010).

Another grain from the same sample, BH12-07B_15a (Fig. 5), shows a network of orthogonal subgrain boundary traces (Fig. 5a–d), which are presumably oriented normal to the Zrn {001} plane. The misorientation axes are parallel to ⟨001⟩ and ⟨100⟩ (Fig. 5e and f) implying the operation of at least two slip systems. Accommodating slip by edge dislocations yields either ⟨100⟩{010} or ⟨010⟩{001} correspondingly. There is also the possibility of a twist boundary when the misorientation axis is parallel to [100], and the corresponding subgrain boundary is (100).

The observation of radial subgrain boundaries may lead to the conclusion that they are cracks, formed due to expansion of the metamicted core. In contrast, in this case the core shows a comparatively high degree of crystallinity (Fig. 5b, colored dots) although heterogeneities due to growth zoning certainly may influence the development of the deformation pattern (see also section Group (III)-3).

Examples described for group (III)-2 show a bright CL signal spatially related with the traces of subgrain boundaries. This may be interpreted as either due to material

SED
6, 1799–1861, 2014

transport and/or higher density of dislocations along the boundaries. Furthermore, both described grains are hosted by biotite. Probably, for this this type of finite deformation pattern a rheologically relatively weak host phase, like for group (III)-1, is favorable, as well as low degree of coupling with the matrix, which causes differential stress within the grain.

However, activation of dominant slip systems in zircon could occur in different tectonic settings as well. The crucial point for this finite deformation pattern to form is such crystallographic orientation with respect to a local stress field, which facilitates crystal-plastic deformation with activation of slip along {100} or {001}. In other words, critical resolved shear stress (CRSS) along the specific glide plane must be reached (Hobbs, 1985).

Crystallographic preferred orientation. One sample, containing zircons with lattice distortion pattern (III)-2, shows CPO of plastically-deformed zircon (sample BH12-07, basic dyke). The Zrn [001] axes of several analyzed grains with finite deformation pattern (III)-2 (e.g. BH12-07B_28; BH12-07A_03a, BH12-07A_04, BH12-07B_31b) are aligned within the foliation plane and parallel to the intersection lineation and fold axis of the sample (Figs. 4 and 9), indicating that crystal-plastic deformation of zircon occurred during folding and contemporaneous shear zone formation. In addition to a similar orientation of C-axis, these grains indicate activation of the slip system ⟨100⟩{010}. All these grains with misorientation axes close to [001], exhibit a similar prismatic shape; grains BH12-07A_03a, BH12-07B_28 and 31b show two symmetrical "lobes" that are displaced along the subgrain boundary tracing from the lower left to the upper right corner of each grain (Figs. 4a and 9a and b).

Two mechanisms for CPO formation could be considered: (a) Dynamic recrystallization by subgrain rotation may have caused systematic lattice rotation. In addition, activation of the dominant slip system is facilitated by a soft host matrix (biotite and chlorite) and/or by decoupling with the matrix. (b) Initial crystallographic orientation of grains in the externally applied stress field facilitates activation of energetically preferable slip systems. Most likely both explanations are appropriate here. In any case CPO

SED
6, 1799–1861, 2014

has not been previously documented for zircon and may need special attention in future studies.

Group III-3, the third group of finite deformation patterns, is characterized by subgrain formation with boundaries emanating from mineral inclusions in zircon (Fig. 6a).

This geometric arrangement of subgrain boundaries could be a result of pinning of dislocations by obstacles during recovery and recrystallization of the crystal lattice (Poirier, 1985). On the other hand, xenocrystic cores, inclusions, pores and cracks within a crystal represent structural heterogeneities, which may induce an inhomogeneous stress distribution (Mancktelow, 2008) and strain localization. Irrespective of whether inclusions have a weaker or stronger rheology than the host grain, stress is heterogeneously distributed in the grain around the mineral inclusion, what may lead to local lattice distortion. The third scenario could be the nucleation of inclusions inside a zircon grain during mylonitization (Kenkmann, 2000), inducing lattice strain and resulting in crystal-plastic deformation of the host phase.

Zircon grain BH12-01B_22 from the ultramylonite core of shear zone 1 shows subgrain boundaries that emanate from a single elliptical mineral inclusion (Fig. 6). Superimposing the traces of subgrain boundaries in the pole figure shows two general families of planes, i.e. one contains the rotation axis and the other is rather normal to it (Fig. 6f). From this observation we infer that the two families of subgrain boundaries represent tilt and twist walls correspondingly. The glide system for the edge dislocations presumably is $\langle -103 \rangle \{30-1\}$. The activation of slip along the high Miller indices plane may be controlled by the inclusion geometry. Grain boundary sliding at the inclusion/host interface may have induced the activation of specific slip planes within the enclosing host (e.g. Raj and Ashby, 1971; Wang et al., 2014).

Another grain that shows subgrain boundaries emanating from a mineral inclusion is BH12-07A_04 (Fig. 9b). The subgrain adjacent to the inclusion (Fig. 9b, marked by arrow) forms due to the presence of differential stress around the inclusion during shearing.

SED
6, 1799–1861, 2014

Group III-4 is a deformation pattern controlled by the microstructure of the host phase, i.e. phase-, grain- or subgrain boundary structure of the host. As the applied differential stress is transferred to the zircon by the host phase, there seems to be a relationship between the zircon subgrain boundary geometry and host (sub)grain boundary geometry, especially in case of strong coupling. (Sub)grain boundaries of the host grain(s) can be often traced inside the hosted zircon grain as subgrain boundaries or brittle cracks.

For example, BH12-04_11 shows the traces of (sub)grain boundaries in the host mineral intersecting the zircon phase boundary at the same sites as zircon subgrain boundaries (elongated grain in Fig. 7a and d, white and black arrows) or cracks (isometric grain, Fig. 7a and d, grey arrow). Subgrain boundaries in elongated zircon BH12-04_11 relate to crystal-plastic deformation by subgrain rotation, that is indicated by the misorientation axes density distribution demonstrating a well-defined cluster (Fig. 7e). Coupling of zircon with rheologically strong host mineral prevents the activation of energetically preferable slip systems in zircon and therefore causes the formation of high indexed misorientation axes. This grain does not demonstrate any visible bright CL features corresponding to the subgrain boundaries. Crystal-plastic deformation therefore resulted in an only insignificant effect on the zircon composition.

Group III-5 is characterized by zircons, where (sub)grain boundaries formed due to initially cataclastic zircon behavior and subsequent crack-healing, as in the sample BH12-02_45. In this case traces of former cracks are clearly shown as bright CL-domains and are often decorated by inclusions or pores (Fig. 8b and d). Despite of the unsystematic scattering of data in the pole figure (Fig. 8f) the misorientation density distribution diagram displays some systematic orientations (Fig. 8e). The misorientation axes are clustered around the Zrn [113], [111] and [311] directions. The orientation of the subgrains within a cluster changes progressively as shown by false color highlighting of the misorientation with respect to a single reference point from 0° = blue (top, Fig. 8a) to 26° = red (bottom, Fig. 8a). This deformation pattern reflects the mylonitization process taking place within the high-temperature shear zones. Fragments

SED
6, 1799–1861, 2014

of large grains may represent the origin of fine-grained zircon found in ultramylonite, characterized by a dark CL-core and a thin bright outer rim (Fig. 6b).

This type of finite deformation patterns predominates in amphibolite-facies rocks, which were affected by intensive fluid circulation that induced crack-healing by material precipitation. Cataclastic behavior of the grain can occur due to very high strain rates, or low temperatures, and/or unfavorable orientation to the local stress field, preventing slip activation.

7.3 CL imaging and Raman spectroscopy

Subgrain boundaries resulting from deformation type (III) often demonstrate a brighter CL signal than the dislocation-free domains (Figs. 3b, 4b, 5b, and 8b). A bright CL response, linked to deformation features, has been already described in the literature (Piazolo et al., 2012; Timms and Reddy, 2009). It has been shown repeatedly that ductile deformation-related microstructures in zircon associated with compositional changes often influence the CL signal (Reddy et al., 2006, 2007; Timms et al., 2006). Therefore, a bright CL-signal is attributed not only to a high dislocation density, but also to a potential trace element enrichment/depletion along the subgrain boundaries, which is supposedly capable of disturbing the isotopic system of the bulk grain (Moser et al., 2009; Timms et al., 2006, 2011).

The results of Raman spectroscopy do not indicate any ductile deformation-related metamictization of zircons that belongs to type (III) deformation patterns. The dislocation density within the subgrains of type (III) is rather low due to recovery and subgrain-rotation recrystallization. In contrast, zircons from granulite facies rocks contain homogeneously distributed dislocations within specific grain domains (IV12-06C_05, type II) or within the entire grain (IV12-06C_16, type I) leading to a decreased degree of crystallinity.

SED
6, 1799–1861, 2014

8 Discussion

Based on several natural examples we have demonstrated the variety of finite deformation patterns of plastically deformed zircons. The investigated zircon grains – when deformed – show either high but coherent lattice strain without dislocation accumulation in (sub)grain boundaries (distortion type I), recrystallization by a polygonization (distortion type III), or a combination of both (type II). The variety of finite deformation patterns is caused by different deformation regimes operating in the material during ductile deformation of the host rocks. Deformation regime of minerals depends on their properties at the given environmental conditions. Following agents that may control the crystal-plastic deformation in zircon are discussed below.

8.1 Temperature

Increase of temperature usually causes softening of the material (e.g. Ranalli, 1995). On the micro-scale, the distortion pattern of the deformed grains is a result of crystal plastic deformation at non-zero volumetric strain that may be accommodated by various temperature-dependent deformation mechanisms (Poirier, 1985; Ranalli, 1995). These deformation mechanisms are, for example, diffusion of vacancies, solution-precipitation, dislocation formation and motion by glide and climb, grain boundary sliding, etc. (Poirier, 1985). Recovery and recrystallization usually act contemporaneously and reduce the dislocation density in the subgrain volume. The difference in finite deformation patterns can result from various combinations of temperature-dependent deformation mechanisms that are operating under certain conditions and in given environment. Decreasing the temperature of deformation (or increasing the strain rate) may induce cataclastic material behavior. That is why in natural rocks crystal-plastic deformation is often coupled with brittle fractures (Grange et al., 2013).

SED
6, 1799–1861, 2014

8.2 Differential stress

Another parameter that can influence the deformation is the magnitude, distribution and direction of applied stress. GNDs form under lithostatic pressure and applied differential stress, therefore, the dislocation density in the deformed crystal is stress-dependent (Ranalli, 1995). However, rise of differential stress causes mechanical hardening of the material by producing more and more dislocations, thus counteracting the effects of high temperature. The differential stress is also a regulating agent for dislocation creep regime, as it controls the dislocation-glide velocity (Ranalli, 1995).

The orientation of differential stress with respect to the lattice orientation also influences the crystal-plastic behavior. The strength of a crystal depends not only on its material properties and environment, but also on its orientation with respect to the externally applied stress field (Ranalli, 1995). If loading is applied parallel to a certain crystallographic plane and deformation conditions are achieved at that plane, in-plane slip systems can be activated (Dahlberg et al., 2014). As we have demonstrated, specific crystallographic orientation relative to the local stress field causes glide along Miller low-indices planes (Figs. 4 and 9), which activates energetically preferable slip systems.

As shown by Kenkmann (2000) and Schmid and Podladchikov (2005), simple shear causes an inhomogeneous spatial distribution of pressure (Schmid and Podladchikov, 2005) and differential stress (Kenkmann, 2000) within a viscous clast decoupled from matrix. This, in turn, causes an inhomogeneous distribution of strain inside the clast. We have demonstrated that these agents in some cases lead to the localized lattice distortion of specific zircon domains. The result of localized differential stress can be seen, for example, in finite deformation types (II), (III)-1 and (III)-2. In type (II) this is caused by grain collision with a rheologically stronger phase, the additional evidences of high differential stress operating in the rock are broken garnets and fine-grained quartz in the host rock. For types (III)-1 and (III)-2 differential stress in zircon appears because of grain-matrix decoupling. Specific grain shape orientation in a local stress

SED
6, 1799–1861, 2014

field induces applied differential stress in specific grain domains (type (III)-1); specific crystallographic orientation in a stress field induces applied differential stress on certain crystallographic planes (type (III)-2).

We suggest that grain BH12-07A_04 (Fig. 9b) represents a natural example for the 2-D models of heterogeneous stress distribution within an elliptical inclusion (Schmid and Podladchikov, 2005). The portions of grain BH12-07A_04 that are rotated correspond spatially to the portions of modeled clast affected by high pressure (differential stress). The growth of the titanite next to zircon boundary (Fig. 9b, Ttn) spatially corresponds to pressure shadow in the models.

8.3 Strain and strain rate

Strain is the response of material to external perturbation as mechanical stress. The shear strain rate is dependent on the shear stress and the material viscosity under the given temperature and tectonic pressure. At the thin section scale the strain is inhomogeneously distributed among the phases and rock domains. However, histograms, showing the distribution of deformed grains across the shear zone profiles (Fig. 14a and b), demonstrate that the more strained rocks contain higher ratio of deformed zircon grains. Thus we observe the positive correlation between the strain of the host rock and amount of hosted strained zircon grains.

8.4 Host environment

Based on the new data, coupling with host matrix together with the rheology of local host environment are considered to be the most important agents controlling the zircon distortion. Viscosity ratio between host and inclusion define the external stress magnitude that the host phase transfers to the inclusion. Furthermore, the strength of coupling between clast and matrix influences the differential stress distribution within the clast (Kenkmann, 2000) and thus may affect finite deformation pattern. When a single grain is deformed being enclosed by a rheologically strong phase and/or strongly cou-

SED
6, 1799–1861, 2014

pled with the matrix, there is no differential stress within the grain (Mancktelow, 2008). In this case active glide planes of the grain are controlled by the host phase, and unfavorable slip planes are activated in zircon (type (III)-4). In addition, zircon often forms subgrain boundaries, which correlate with host mineral deformation features (e.g. type (III)-4). According to Kenkmann (2000), clasts that are well coupled with the matrix can also demonstrate high amount of defects, concentrated at the rim. This picture we see for grain IV12-06C_05, or distortion patterns type (II).

In cases where the host phase is rheologically significantly weaker than the inclusion, and/or where the clast is decoupled from the matrix, the differential stress occurs within the clast. For example, crystal-plastic deformation of zircon decoupled from mica host results in activation of dominant slip systems related to the elementary crystallographic axes [100], [010] and [001] (type (III)-2). One sample even points to the formation of a crystallographic preferred orientation (CPO) presumably due to dynamic recrystallization of zircon by subgrain rotation in the soft mica matrix (Figs. 4 and 9).

8.5 Presence of water

The presence or absence of water in the system during metamorphism seems to influence the finite deformation pattern. Previous studies have shown that crystals deformed under anhydrous conditions are usually much stronger than crystals under wet conditions ("hydrolithic weakening", e.g. Ranalli, 1995). Water presence during amphibolite-facies deformation of rocks from Tauern Window could be among the reasons for well-developed subgrain boundaries in zircon (deformation pattern type III), whereas dry deformation conditions of rocks from the Ivrea-Verbano Zone did not induce formation of such features. Fluid presence is also supposed to have caused the higher content of deformed and hydrothermally-recrystallized zircons in gneisses from Tauern Window. However, majority of deformed zircons from Tauern Window represent deformation pattern type (III)-5 which is a result of brittle deformation.

SED
6, 1799–1861, 2014

8.6 Crystal anisotropy

Crystal-plastically deformed zircon grains often demonstrate orientations of slip direction, slip plane, rotation axis and subgrain boundaries parallel to crystallographic directions and planes with low Miller's indices.

The elastic anisotropy of zircon can be visualized by constraining *P* wave velocity contours and Young's modulus contours (Fig. 14d and e). The high values for both parameters are parallel to Zrn {100} and the highest value is in the basal plane Zrn {001}. High *P* wave velocity values along the planes indicate that these planes are most densely occupied in the crystal structure. Slip takes place parallel to these planes, because it is preferred in the direction, where the atoms are most closely spaced (Poirier, 1985). The densest plane is the basal plane {001}, and deformed grains most often have a rotation axis parallel to [001] (Fig. 14c). High Young's modulus values along the planes of low Miller's indices indicate that the material along these crystallographic planes is less elastic. This elastic anisotropy results in preferable activation of slip systems ⟨100⟩{010}, ⟨010⟩{001} and ⟨001⟩{010}.

Other sources of crystal anisotropy could be: growth zoning, inclusions, cracks, pores. They produce weaknesses in the crystal structure and infer an inhomogeneous stress distribution.

Finite deformation patterns types (III)-2 and (III)-3 can be generally described as deformation that follows the internal mechanical weakness of the zircon crystal structure. In the first case the "weak" zones are crystallographic heterogeneities related to the lattice properties of zircon; and in the second case the source of internal anisotropy are the mineral inclusions.

8.7 Grain shape

As we have shown, favorable orientation of grain shape with respect to applied stress can indicate specific deformation pattern (type (III)-2), on conditions that grain is decoupled from the matrix.

SED
6, 1799–1861, 2014

Grains indicating a crystallographic preferred orientation in sample BH12-07 (Figs. 4 and 9) all have a similar grain shape, that probably also induced specific crystal-plastic deformation mechanisms together with decoupling from the matrix. In sample IV12-06C zircon grains with isometric roundish shape appear to be undeformed, whereas crystal plastic deformation features are restricted to irregularly-shaped grains (Figs. 10 and 12). This is consistent with above mentioned inhomogeneous stress and strain distributions during deformation, caused by specific grain shape.

8.8 Distribution of misorientation axes

All listed agents are interconnected and often combined. Based on 60 deformed grains investigated for the current study, the density distribution of the misorientation axes have been plotted, resulting in 6 distinct areas in the pole figure (Fig. 14c). In the most common case, misorientation axes are spread around the ⟨001⟩ direction; a large group of misorientation axes is located around ⟨320⟩ and orientation clusters around ⟨100⟩ and ⟨111⟩. Less common, the misorientation axes are clustered around ⟨201⟩ and ⟨203⟩. So, the misorientation axes do not necessarily occupy favorable rotation axes ⟨001⟩ and ⟨100⟩ (Reddy et al., 2007), but can be activated in different crystal directions, controlled by a number of agents that influence the mechanical behavior of the system.

Grains hosted by biotite or fine-grained matrix mostly belong to areas around ⟨001⟩ and ⟨100⟩, whereas grains hosted by feldspars preferably occupy areas around ⟨110⟩, ⟨210⟩ and ⟨311⟩. This regularity demonstrates that the ratio between clast and matrix viscosities may control slip in the clast. The higher is this ratio, the less is degree of mechanical coupling, the higher is the probability of activation of the dominant or energetically-preferable slip systems in the clast.

8.9 Zircon deformation model

We propose the general model of zircon crystal-plastic deformation, based on comparison of rheological behavior of zircon with various distortion patterns. The schematic

SED
6, 1799–1861, 2014

diagram of stress-strain curves proposed for different finite deformation patterns of zircon is shown in the Fig. 15.

According to empirical observations, strain is decreasing from grains with distortion patterns type (I) to grains with patterns type (III). For type (I) strain is comparatively high, the c-axis of the grain IV12-06C_16 is normal to elongation, what is untypical for zircon, and the grain shape is highly euhedral. For patterns type (II) strain is also rather high, but it is localized within certain domains. The bright CL rim of the grain IV12-06C_05 is significantly reduced in thickness where grain is distorted. Strain is comparatively low for zircon grains deformed resulting in distortion patterns type (III). The grains have idiomorphic or subidiomorphic shapes that are generally not distorted, except of deformation pattern (III)-5, which is considered not to be a result of crystal-plastic deformation.

With empirical observations we can also attempt to evaluate comparative differential stress for distortion patterns. Most likely, stress is decreases from patterns type (I) to patterns type (III), based on amount and character of dislocation creep and recovery.

If the differential stress is comparatively high, the strain rate at the initial stage of deformation is comparatively high. GDNs are produced fast overall within the grain, so their density increases and soon they become tangled with no opportunity to move. Thus, in this scenario we expect no dislocation creep and, therefore, no grain recovery soon after deformation begins. Grain is gradually bending, resulting in the deformation patterns type (I). If the stress remains high, the strain rate becomes lower, and the increasing density of GNDs will eventually result in strain hardening and in brittle deformation (Ranalli, 1995).

At comparatively lower differential stress and lower strain, the strain rate increasing and then become constant. The dislocation creep is operating, but GDNs are produced faster than they are removed or recovered. More and more stress-induced dislocations appear and move towards the subgrain boundaries, but some of them remain in the subgrains and cause gradual bending of the grain domains. Eventually, subgrain rotation leads to high-angle boundary formation and grain size reduction. Newly formed

SED
6, 1799–1861, 2014

grains are supposed to be strain-free, whereas the parent grain continues to deform. This scenario results in deformation patterns *type (II)*. If the differential high stress and resulting high strain rate continue to operate, we expect complete recrystallization of the grain into a fine-grain aggregate.

At moderate differential stress and comparatively low strain, GDNs are also expected to form, to glide and to climb. By dislocation glide well-defined subgrain walls are formed; and by dislocation climb subgrains are recovered. The rate of dislocation formation is lower, or at least the same that the rate of dislocation recovery. As a result, we observe subgrain rotation recrystallization, or poligonization, which is represented in deformation patterns *type (III)*. If strain rate at low strain becomes constant, it may establish the conditions that are close to steady-state dislocation creep (e.g. Gleason and Tullis, 1995), especially under the fluid presence.

Essentially, the ratio between the *rate of dislocations formation* and the *rate of dislocations motion* is responsible for the variety of lattice distortion patterns that are observed. The ratio between syntectonic metamorphic temperature conditions and the strain rate defines whether dislocations can migrate faster than they are generated, or whether they remain dispersed within the crystal lattice (Ranalli, 1995). So, in the end, it is temperature and shear stress that mainly control the type of zircon lattice distortion pattern.

9 Conclusions

The detailed investigation of the deformation behavior of fine-grained zircon in association with the host phases provides important new information on the zircon rheology in common metamorphic settings:

1. During deformation at amphibolite – granulite facies metamorphic conditions fine-grained zircon behaves rheologically identical to coarse-grained zircon (compared with e.g. Reddy et al., 2007; Piazolo et al., 2012).

SED
6, 1799–1861, 2014

2. New microstructural and textural data describe three clearly distinguished crystal-plastic distortion patterns of zircon. Type (I) distortion patterns are characterized by comparatively large intra-granular orientation variations, although subgrains and subgrain boundaries are absent. Type (II) distortion patterns are indicated by gradual bending of the crystal lattice coupled with (sub)grain boundary formation exhibiting concentric shape and significant intragranular misorientation. Distortion patterns of type (III) show the formation of well-defined low-angle boundary networks separating strain-free subgrains.

3. Difference in finite deformation patterns of zircon is considered to be dependent on the ratio between the rate of dislocations formation and the rate of dislocations motion. This ratio is mainly controlled by local differential stress and temperature.

4. Zircon crystal-plastic deformation behavior is mainly controlled by the following agents: temperature-dependent dislocation creep, magnitude and orientation of the local stress field with respect to the zircon lattice orientation and grain shape, host phase(s) rheology, degree of coupling with the matrix, fluid presence and internal mechanical anisotropy. Among these agents the coupling with the matrix and zircon crystal anisotropy play the leading roles.

5. Due to elastic anisotropy of zircon, slip in zircon preferably occurs along the low-indexed crystallographic directions ⟨100⟩ and ⟨001⟩, and parallel to the most densely packed planes {010} and {001}. In favorable cases (e.g. when the viscosity ratio between grain and matrix is large) the following energetically-preferable slip systems in zircon are active: ⟨100⟩{010}, ⟨010⟩{001} and ⟨001⟩{010}.

6. When the viscosity ratio between grain and matrix is low, and/or when the grain is strongly coupled with its host, unfavorable slip along the high indexed crystallographic planes and unfavorable slip systems can be activated.

SED
6, 1799–1861, 2014

7. Hydrothermal alteration of zircon does not obviously induce or influence crystal-plastic deformation, although in some cases a temporal and spatial relationship between those two processes can be inferred.

Acknowledgements. This study was funded by the University of Vienna (doctoral school "DOGMA", project IK 052) and the Austrian Science Foundation Fund (FWF): I471-N19, which is part of the DFG-FWF funded international research group FOR741-DACH.

The authors are grateful to Rainer Abart, Christian Auer, Claudia Beybel, Franz Biedermann, Bernhard Grasemann, Sigrid Hrabe, Matthew Huber, Hugh Rice, Claudia Trepmann, and all colleagues of the FOR741 research group for fruitful discussions and the Geologische Bundesanstalt (GBA) of Austria for access to the SEM.

References

Akchurin, M. S., Zakalyukin, R. M., Kaminsky, A. A., and Kupenko, I. I.: Role of twinning in plastic deformation, Crystallogr. Rep., 55, 621–625, 2010.

Bachmann, F., Hielscher, R., and Schaeben, H.: Texture analysis with MTEX – free and open source software toolbox, Sol. St. Phen., 160, 63–68, 2010.

Bachmann, F., Hielscher, R., and Schaeben, H.: Grain detection from 2d and 3d EBSD data-specification of the MTEX algorithm, Ultramicroscopy, 111, 1720–1733, 2011.

Barboza, S. A., Bergantz, G. W., and Brown, M.: Regional granulite facies metamorphism in the Ivrea zone: is the Mafic Complex the smoking gun or a red herring?, Geology, 27, 447–450, 1999.

Bass, J. D.: Elasticity of minerals, glasses and melts, in: Mineral Physics and Crystallography: a Handbook of Physical Constants, edited by: Ahrens, T. J., American Geophysical Union, Washington, DC, 45–63, 1995.

Brodie, K. H., Rutter, E. H., and Evans, P.: On the structure of the Ivrea-Verbano Zone (northern Italy) and its implications for present-day lower continental crust geometry, Terra Nova, 4, 34–39, 1992.

Cherniak, D. J. and Watson, E. B.: Diffusion in Zircon, in: Zircon, edited by: Hanchar, J. M. and Hoskin, P. W. O., Reviews in Mineralogy and Geochemistry, vol. 53, Mineralogical Society of America and Geochemical Society, Washington, DC, 113–143, 2003.

SED

6, 1799–1861, 2014

Cherniak, D. J., Lanford, W. A., and Ryerson, F. J.: Lead diffusion in apatite and zircon using ion implantation and Rutherford Backscattering techniques, Geochim. Cosmochim. Ac., 55, 1663–1673, 1991.

Corfu, F., Hanchar, J. M., Hoskin, P. W. O., and Kinny, P.: Atlas of zircon textures, in: Zircon, edited by: Hanchar, J. M. and Hoskin, P. W. O., Reviews in Mineralogy and Geochemistry, vol. 53, Mineralogical Society of America and Geochemical Society, Washington, DC, 468–500, 2003.

Dahlberg, C. F. O., Saito, Y., Öztop, M. S., and Kysar, J. W.: Geometrically necessary dislocation density measurements associated with different angles of indentations, Int. J. Plasticity, 54, 81–95, 2014.

Davis, D. W., Williams, I. S., and Krogh, T. E.: Historical development of zircon geochronology, in: Zircon, edited by: Hanchar, J. M. and Hoskin, P. W. O., Reviews in Mineralogy and Geochemistry, vol. 53, Mineralogical Society of America and Geochemical Society, Washington, DC, 145–181, 2003.

Flowers, R. M., Schmitt, A. K., and Grove, M.: Decoupling of U–Pb dates from chemical and crystallographic domains in granulite facies zircon, Chem. Geol., 270, 20–30, 2010.

Geisler, T., Ulonska, M., Schleicher, H., Pidgeon, R. T., and Van Bronswijk, W.: Leaching and differential recrystallization of metamict zircon under experimental hydrothermal conditions, Contrib. Mineral. Petr., 141, 53–65, 2001.

Geisler, T., Kurtz, R., Pidgeon, R. T., and van Bronswijk, W.: Transport of uranium, thorium and lead in metamict zircon under low-temperature hydrothermal conditions, Chem. Geol., 191, 141–154, 2002.

Geisler, T., Pidgeon, R. T., Kurtz, R., Bronswijk, W., and Schleicher, H.: Experimental hydrothermal alteration of partially metamict zircon, Am. Mineral., 88, 1496–1513, 2003.

Gleason, G. C. and Tullis, J.: A flow law for dislocation creep of quartz aggregates determined with the molten salt cell, Tectonophysics, 247, 1–23, 1995.

Goetze, J., Ploetze, M., and Habermann, D.: Origin, spectral characteristics and practical applications of the cathodoluminescence (CL) of quartz – a review, Miner. Petrol., 71, 225–250, 2001.

Grange, M. L., Pidgeon, R. T., Nemchin, A. A., Timms, N. E., and Meyer, C.: Interpreting U–Pb data from primary and secondary features in lunar zircon, Geochim. Cosmochim. Ac., 101, 112–132, 2013.

SED
6, 1799–1861, 2014

Hobbs, B. E.: The geological significance of microfabric analysis, in: Preferred Orientation in Deformed Metal and Rocks. An Introduction to Modern Texture Analysis, edited by: Wenk, H. R., Elsevier Inc., 463–484, 1985.
Kenkmann, T.: Processes controlling the shrinkage of porphyroclasts in gabbroic shear zones, J. Struct. Geol., 22, 471–487, 2000.
MacDonald, J. M., Wheeler, J., Harley, S. L., Mariani, E., Goodenough, K. M., Crowley, Q., and Tatham, D.: Lattice distortion in a zircon population and its effects on trace element mobility and U–Th–Pb isotope systematics: examples from the Lewisian Gneiss Complex, northwest Scotland, Contrib. Mineral. Petr., 166, 21–41, 2013.
Mainprice, D., Hielscher, R., and Schaeben, H.: Calculating anisotropic physical properties from texture data using the MTEX open source package, in: Deformation Mechanisms, Rheology and Tectonics: Microstructures, Mechanics and Anisotropy, in: Prior, D. J., Rutter, E. H., and Tatham, D. J., Special Publications, vol. 360, Geological Society, London, 175–192, 2011.
Mancktelow, N. S.: Tectonic pressure: theoretical concepts and modelled examples, Lithos, 103, 149–177, 2008.
Mancktelow, N. S.: Behaviour of an isolated rimmed elliptical inclusion in 2-D slow incompressible viscous flow, J. Struct. Geol., 46, 235–254, 2013.
Miller, C., Konzett, J., Tiepolo, M., Armstrong, R. A., and Thöni, M.: Jadeite-gneiss from the eclogite zone, Tauern Window, Eastern Alps, Austria: metamorphic, geochemical and zircon record of a sedimentary protholith, Lithos, 93, 68–88, 2007.
Moser, D. E., Davis, W. J., Reddy, S. M., Flemming, R. L., and Hart, R. J.: Zircon U–Pb strain chronometry reveals deep impact-triggered flow, Earth Planet. Sc. Lett., 277, 73–79, 2009.
Moser, D. E., Cupelli, C. L., Barker, I. R., Flowers, R. M., Bowman, J. R., Wooden, J., and Hart, J. R.: New zircon shock phenomena and their use for dating and reconstruction of large impact structures revealed by electron nanobeam (EBSD, CL, EDS) and isotopic U–Pb and (U–Th)/He analysis of the Vredefort dome, Can. J. Earth Sci., 48, 117–139, 2011.
Nye, J. F.: Some geometrical relations in dislocated crystals, Acta Metall. Mater., 1, 153–162, 1953.
Pennacchioni, G. and Mancktelow, N. S.: Nucleation and initial growth of a shear zone network within compositionally and structurally heterogeneous granitoids under amphibolite facies conditions, J. Struct. Geol., 29, 1757–1780, 2007.

SED
6, 1799–1861, 2014

Piazolo, S., Austrheim, H., and Whitehouse, M.: Brittle-ductile microfabrics in naturally deformed zircon: deformation mechanisms and consequences for U-Pb dating, Am. Mineral., 97, 1544–156, 2012.

Poirier, J. P.: Creep of Crystals: High-Temperature Deformation Processes in Metals, Ceramics and Minerals, Cambridge Earth Science Series, edited by: Cook, A. H., Harland, W. B., Hughes, N. F., Putnis, A., Sclater, J. G., and Thomson, M. R. A., Cambridge University Press, Leipzig, 260 pp., 1985.

Quick, J. E., Sinigoi, S., Peressini, G., Demarchi, G., Wooden, J. L., and Sbisà, A.: Magmatic plumbing of a large Permian caldera exposed to a depth of 25 km, Geology, 37, 603–606, 2009.

Raj, R. and Ashby, M. F.: On grain boundary sliding and diffusional creep, Metall. Trans., 2, 1113–1127, 1971.

Ranalli, G.: Rheology of the Earth, 2nd edn., Chapman & Hall, London, 413 pp., 1995.

Reddy, S. M. and Timms, N. E.: Deformation of Zircon and Implications for Geochemistry and Geochronology, Source Abstracts with Programs, vol. 42, Geol. Soc. Am., 634 pp., 2010.

Reddy, S. M., Timms, N. E., Trimby, P., Kinny, P. D., Buchan, C., and Blake, K.: Crystal-plastic deformation of zircon: a defect in the assumption of chemical robustness, Geology, 34, 257–260, 2006.

Reddy, S. M., Timms, N. E., Pantleon, W., and Trimby, P.: Quantitative characterization of plastic deformation of zircon and geological implications, Contrib. Mineral. Petr., 153, 625–645, 2007.

Reddy, S. M., Timms, N. E., Hamilton, P. J., and Smyth, H. R.: Deformation-related microstructures in magmatic zircon and implications for diffusion, Contrib. Mineral. Petr., 157, 231–244, 2009.

Redler, C., Johnson, T. E., White, R. W., and Kunz, B. E.: Phase equilibrium constraints on a deep crustal metamorphic field gradient: metapelitic rocks from the Ivrea Zone (NW Italy), J. Metamorph. Geol., 30, 235–254, 2012.

Roters, F., Eisenlohr, P., Hantcherli, L., Tjahjanto, D. D., Bieler, T. R., and Raabe, D.: Overview of constitutive laws, kinematics, homogenization and multiscale methods in crystal plasticity finite-element modeling: theory, experiments, applications, Acta Mater., 58, 1152–1211, 2010.

Rutter, E. H., Brodie, K. H., James, T., and Burlini, L.: Large-scale folding in the upper part of the Ivrea-Verbano zone, NW Italy, J. Struct. Geol., 29, 1–17, 2007.

SED
6, 1799–1861, 2014

Schwartz, J. J., John, B. E., Cheadle, M. J., Wooden, J. L., Mazdab, F., Swapp, S., Craig, B., and Grimes, C. B.: Dissolution–reprecipitation of igneous zircon in mid-ocean ridge gabbro, Atlantis Bank, Southwest Indian Ridge, Chem. Geol., 274, 68–81, 2010.

Schmid, D. W. and Podladchikov, Y. Y.: Are isolated stable rigid clasts in shear zones equivalent to voids?, Tectonophysics, 384, 233–242, 2004.

Schmid, D. W. and Podladchikov, Y. Y.: Mantled porphyroclast gauges, J. Struct. Geol., 27, 571–585, 2005.

Selverstone, J.: Petrologic constraints on imbrication, metamorphism, and uplift in the SW Tauern Window, Eastern Alps, Tectonics, 4, 687–704, 1985.

Selverstone, J., Morteani, G., and Staude, J.-M.: Fluid channelling during ductile shearing: transformation of granodiorite into aluminous schist in the Tauern Window, Eastern Alps, J. Metamorp. Geol., 9, 419–431, 1991.

Sinigoi, S., Quick, J. E., Demarchi, G., and Klötzli, U.: The role of crustal fertility in the generation of large silicic magmatic systems triggered by intrusion of mantle magma in the deep crust, Contrib. Mineral. Petr., 162, 691–707, 2011.

Sturm, R. and Steyrer, H. P.: Use of accessory zircon for the quantification of volume changes in ductile shear zones cutting plutonic rocks, Chem. Erde-Geothem., 63, 31–54, 2003.

Timms, N. E. and Reddy, S. M.: Response of cathodoluminescence to crystal-plastic deformation in zircon, Chem. Geol., 261, 11–23, 2009.

Timms, N. E., Kinny, P., and Reddy, S. M.: Enhanced diffusion of uranium and thorium linked to crystal plasticity in zircon, Geochem. T., 7, 10, doi:10.1186/1467-4866-7-10, 2006.

Timms, N. E., Kinny, P., Reddy, S. M., Evans, K., Clark, C., and Healy, D.: Relationship among titanium, rare earth elements, U–Pb ages and deformation microstructures in zircon: implications for Ti-in-zircon thermometry, Chem. Geol., 280, 33–46, 2011.

Timms, N. E., Reddy, S. M., Healy, D., Nemchin, A. A., Grange, M. L., Pidgeon, R. T., and Hart, R.: Resolution of impact-related microstructures in lunar zircon: a shock-deformation mechanism map, Meteorit. Planet. Sci., 47, 120–141, 2012.

Veselá, P., Söllner, F., Finger, F., and Gerdes, A.: Magmato-sedimentary Carboniferous to Jurassic evolution of the western Tauern window, Eastern Alps (constraints from U-Pb zircon dating and geochemistry), Int. J. Earth Sci., 100, 993–1027, 2011.

Wang, L., Zhou, J., Zhang, S., Liu, Y., and Dong, S.: Effects of accommodated grain boundary sliding on triple junction nanovoid nucleation in nanocrystalline materials, Mech. Mater., 71, 10–20, 2014.

SED
6, 1799–1861, 2014

Wheeler, J., Mariani, E., Piazolo, S., Prior, D. J., Trimby, P. J., and Drury, M. R.: The weighted Burgers vector: a new quantity for constraining dislocation densities and types using electron backscatter diffraction on 2-D sections through crystalline materials, J. Microsc.-Oxford, 233, 482–494, 2008.

SED
6, 1799–1861, 2014

Table 1. Types of finite deformation patterns with examples from the present study and from literature. Groups characterizing type (III) lattice distortion describe different mechanisms for finite deformation pattern formation observed.

Type (I) gradual bending, no subgrain boundaries		Type (II) both gradual bending and subgrain boundaries		Type (III) network of low-angle boundaries	
Description	Examples	Description and conditions	Examples	Description and conditions	Examples
Free dislocation density, gradual bending of the grain, misorientation axes parallel to [001] or [100].	**IV12-06C_16** (Fig. 12); "type I lattice distortions" in Piazolo et al. (2012); BP03/3 in MacDonald et al. (2013); LG-2a Grain 17 in Moser et al. (2009); area A in Reddy et al. (2007); zircon 5 from 73215,122 in Timms et al. (2012).	Local deformation of the rim(s) due to collision of crystals/mineral grains or deformation within fine-grained matrix; presence of 2 and more misorientation axes often observed. Inhomogeneous pressure distribution required.	**IV12-06C_05** (Figs. 10 and 11); "type II lattice distortions" in Piazolo et al. (2012); GG09/1 in MacDonald et al. (2013); area B and C in Reddy et al. (2007); grain from GST15 (area A) in Timms et al. (2006) and Timms and Reddy (2009); grains 5 and 8 from Jhs2PON4, Timms and Reddy (2009).	**Group 1** Deformation of specific grain domains. Favorable shape orientation in the local stress field; decoupling from the matrix.	**BH12-05B_07** (Fig. 3); DP02/7 in MacDonald et al. (2013); V09-237 G4 in Moser et al. (2011); UX in Timms and Reddy (2009).
				Group 2 Activation of dominant slip system(s). Favorable crystallographic orientation in the local stress field and rheologically weaker host phase required.	**BH12-07A_03a** (Fig. 9a), **BH12-07B_15a** (Fig. 5), **BH12-07B_26** (Fig. 9c), **BH12-07B_28** (Fig. 4), **BH12-07B_31b** (Fig. 9b). Type of distortion III, Piazolo et al. (2012).
				Group 3 Low-angle boundaries emanating from mineral inclusion. Internal heterogeneity required.	**BH12-01B_22** (Fig. 6).
				Group 4 Depends on the configuration of the host phases, coupling with the matrix required.	**BH12-04_11** (Fig. 7), **BH12-07A_03a** (Fig. 9a); BP06/3 in MacDonald et al. (2013) (?).
				Group 5 Brittle deformation, sometimes followed by the crack healing.	**BH12-02_45** (Fig. 8); ST02/2 and Fig. 8b in MacDonald et al. (2013); 5 from 73235,60 in Timms et al. (2012).

SED
6, 1799–1861, 2014

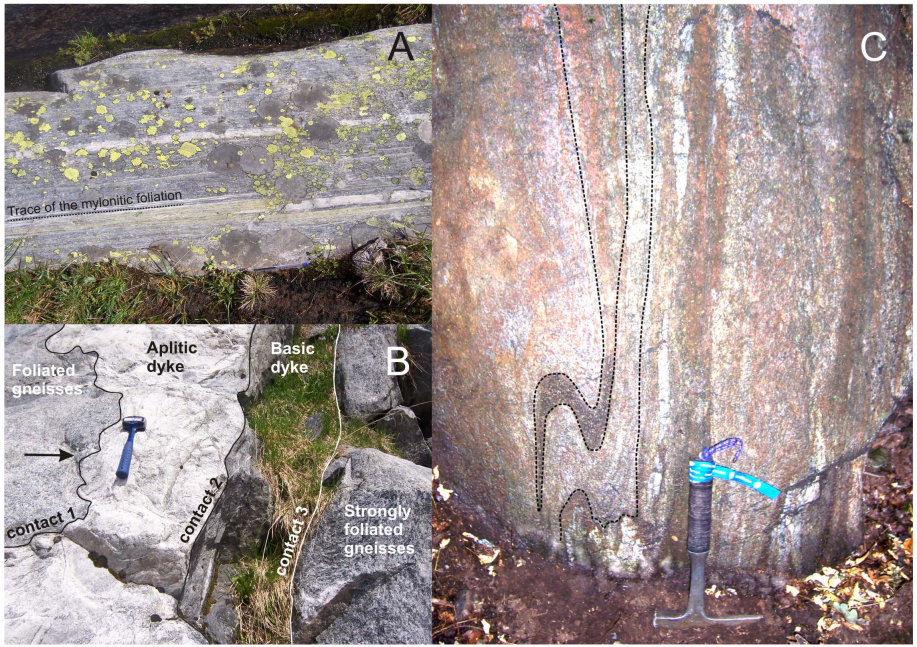

Figure 1. Outcrop photographs. **(A)** Shear zone 1 in orthogneiss with strong mylonitic foliation. **(B)** Shear zone 2 with two dykes hosted by granitic gneiss. Contact 1 shows a cuspate-lobate structure (black arrow). **(C)** Shear zone 3, hosting highly-deformed and folded stronalite. Folds of compositional layering are highlighted by the dashed black lines.

SED
6, 1799–1861, 2014

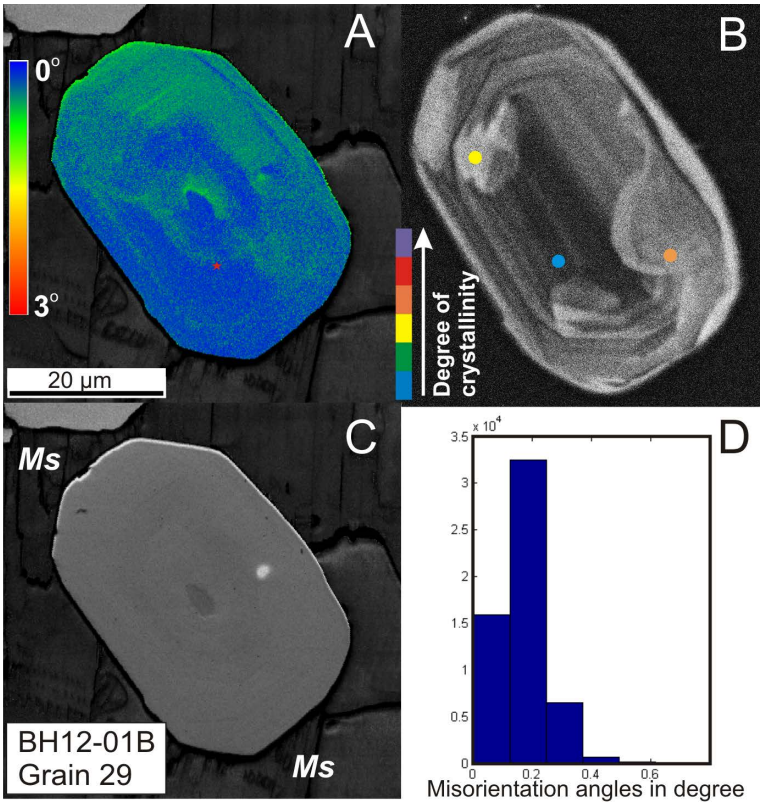

Figure 2. Grain BH12-01B_29. **(A)** EBSD map color coded for zircon misorientation (blue – red = 0–3°) of each pixel relative to a reference point (red star marker). **(B)** CL image with colored points representing relative degrees of crystallinity, measured by Raman spectroscopy. **(C)** EBSD pattern quality map, Ms = muscovite. **(D)** Histogram of the distribution of misorientation angles between neighboring data points.

SED
6, 1799–1861, 2014

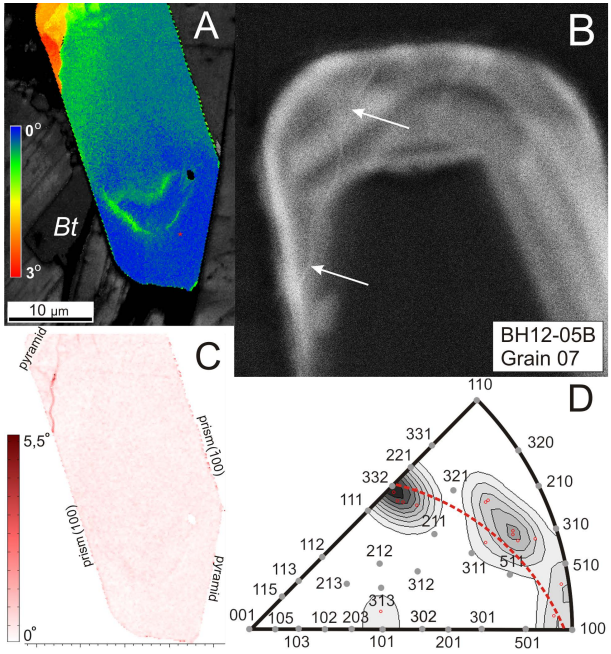

Figure 3. *Grain BH12-05B_07*. **(A)** EBSD map color coded for zircon misorientation with respect to a reference point (red star marker), Bt = biotite; **(B)** detailed CL image of the upper part of the grain, bright trace (marked by white arrows) corresponds to subgrain boundary; **(C)** EBSD map of zircon that shows the orientation changes between neighboring data points ("local misorientation"), labels indicate families of crystallographic faces; **(D)** inverse pole figure plot of the misorientation axes distribution density comprising the positions of misorientation axes (small red circles), crystallographic directions (gray dots) and the great circle formed by the misorientation axes (dashed red line).

SED
6, 1799–1861, 2014

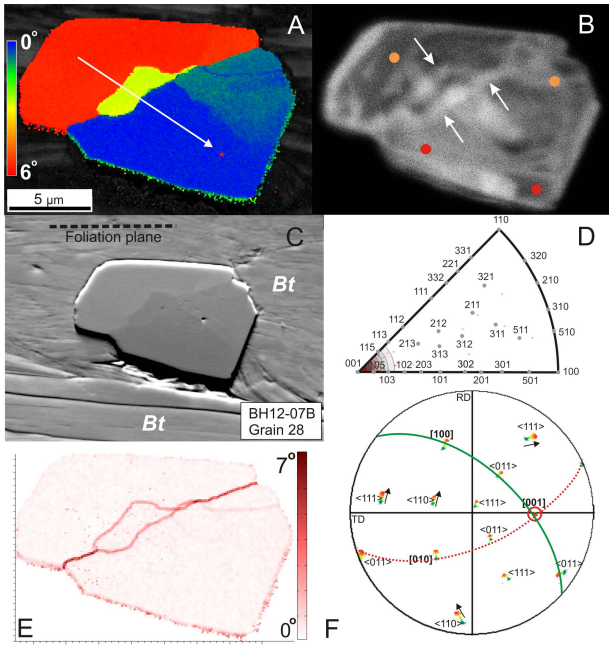

Figure 4. Grain BH12-07B_28. **(A)** EBSD map color coded for zircon misorientation with respect to a reference point (red star marker). The white arrow corresponds to the misorientation profile shown in Fig. 13c; **(B)** CL image, the bright lines (marked by white arrows) correspond to the subgrain boundaries, colored points represent relative degree of crystallinity, color coding is as in Fig. 2b; **(C)** forescatter electron (FSE) image, Bt = biotite. **(D)** Inverse pole figure plot with the distribution density of misorientation axes shows concentration around Zrn [001]. **(E)** EBSD map of zircon showing the misorientation between neighboring data points; **(F)** pole figure plot showing zircon crystal directions (lower hemisphere equal area projection) color coded as in **(A)**. Labels indicate the crystallographic directions. Black arrows show scattering of axes due to rotation about Zrn [001] (red circle). The dashed red line shows the orientation of the subgrain boundary, the solid green line indicates the slip plane orientation.

SED
6, 1799–1861, 2014

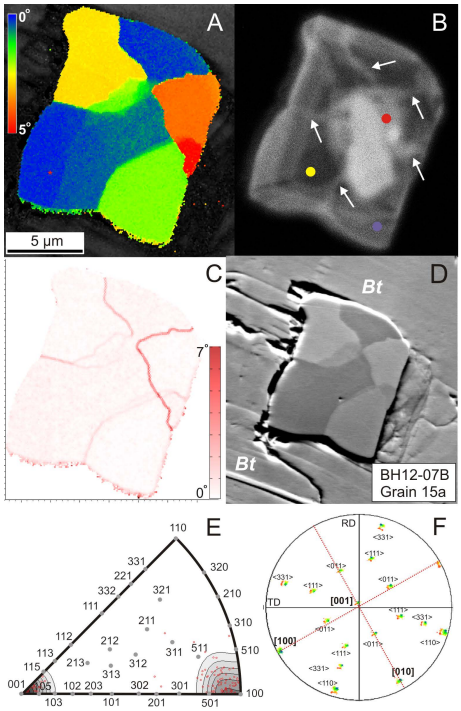

Figure 5. Grain BH12-07B_15a. **(A)** EBSD map color coded for zircon misorientation with respect to a reference point (red star marker); **(B)** CL image; bright traces (marked by white arrows) correspond to subgrain boundaries, colored dots represent the relative degree of crystallinity, color coding as in Fig. 2b; **(C)** EBSD map of zircon showing the misorientation between neighboring data points; **(D)** orientation contrast image (FSE), Bt = biotite. **(E)** Inverse pole figure plot of the distribution density of misorientation axes shows concentrations around ⟨001⟩ and ⟨100⟩. **(F)** Pole figure plot showing zircon crystal directions (lower hemisphere equal area projection) colored as in A. Labels indicate the crystallographic directions. Dashed red lines show the subgrain boundary orientations.

SED
6, 1799–1861, 2014

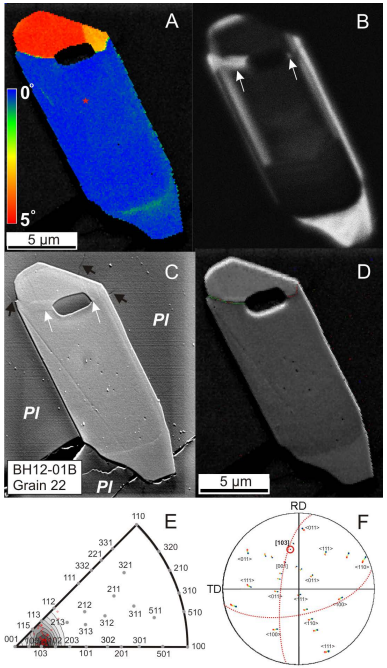

Figure 6. Grain BH12-01B_22. **(A)** EBSD map color coded for misorientation with respect to a reference point (red star marker); **(B)** CL image with bright recrystallization zones (shown by white arrows); **(C)** SE image showing subtle cracks (black arrows) in host plagioclase, and recrystallization zones as in **(B)** (shown by white arrows), Pl = plagioclase; **(D)** EBSD pattern quality map showing subgrain boundaries colored for misorientation angles between subgrains (red lines = 2–3°, green lines = 3–5°). **(E)** Inverse pole figure plot of the misorientation axes distribution density showing concentration around Zrn [103]. **(F)** Pole figure plot showing zircon crystal directions (lower hemisphere equal area projection) colored as in Fig. 6a. Labels indicate the crystallographic directions. Orientation scattering corresponds to rotations around [103] (red circle). Dashed red lines show boundary wall orientations.

SED
6, 1799–1861, 2014

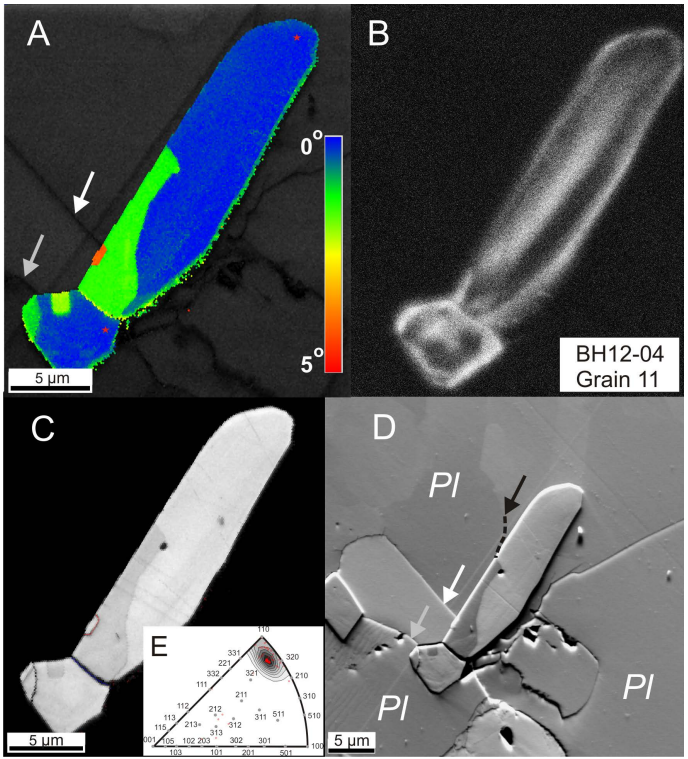

Figure 7. Grain BH12-04_11. **(A)** EBSD map color coded for zircon misorientation with respect to a reference point (red star marker). Arrows mark plagioclase grain boundary segments; **(B)** CL image; **(C)** EBSD pattern quality map with subgrain boundaries colored for misorientation angles between subgrains (red line = 2–5°); **(D)** FSE image (black arrow and dashed line mark plagioclase subgrain boundary, white and grey arrows as in **A**), Pl = plagioclase; **(E)** Inverse pole figure plot of the misorientation axes distribution density shows maxima close to Zrn [320].

SED
6, 1799–1861, 2014

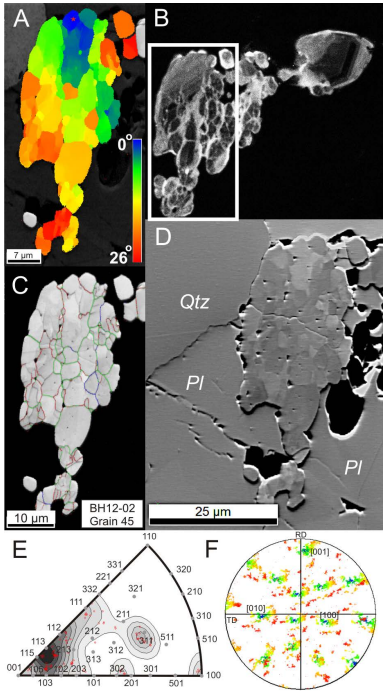

Figure 8. Grain BH12-02_45. **(A)** EBSD map color coded for zircon misorientation with respect to a reference point (red star marker); **(B)** CL image (white rectangle marks position of EBSD map); **(C)** EBSD pattern quality map with subgrain boundaries colored for misorientation angles between subgrains (red = 2°–5°, green = 5°–15°, blue > 15°); **(D)** FSE image, Qtz = quartz, Pl = plagioclase; **(E)** inverse pole figure plot of the misorientation axes distribution density; **(F)** Pole figure plot showing zircon crystal directions (lower hemisphere equal area projection) colored as in **(A)**. Labels indicate the crystallographic directions.

SED
6, 1799–1861, 2014

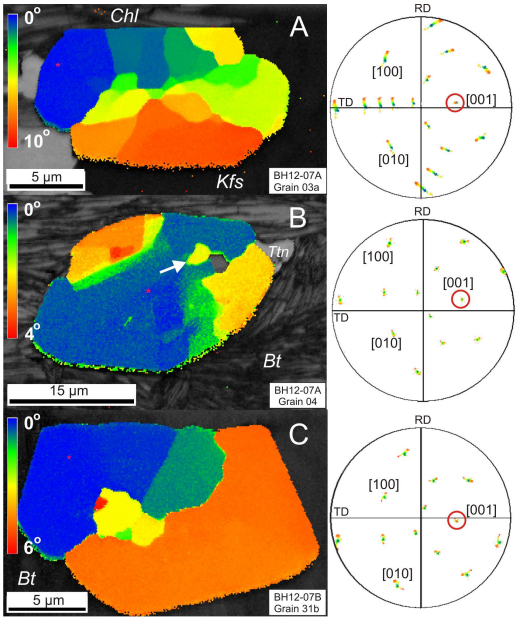

Figure 9. (Sub)grain shape and crystallographic orientation of zircon from sample BH12-07 (basic dyke). Left hand side – EBSD maps colored for misorientation with respect to a single reference point (red star marker), right hand side – pole figure plots showing zircon crystal directions (lower hemisphere equal area projection) colored as the corresponding EBSD map. Rotation axes parallel to Zrn [001] are highlighted by a red circle. **(A)** Grain BH12-07A_03a; **(B)** grain BH12-07A_04, arrow highlights subgrain adjacent to the mineral inclusion; **(C)** grain BH12-07B_31B; Bt = biotite, Chl = chlorite, Kfs = K-feldspar, Ttn = titanite. NB! The thin sections were cut normal to the foliation plane and at an angle of 50° with respect to the intersection lineation, so that the Zrn [001] direction coincides with the intersection lineation and the fold axis.

SED
6, 1799–1861, 2014

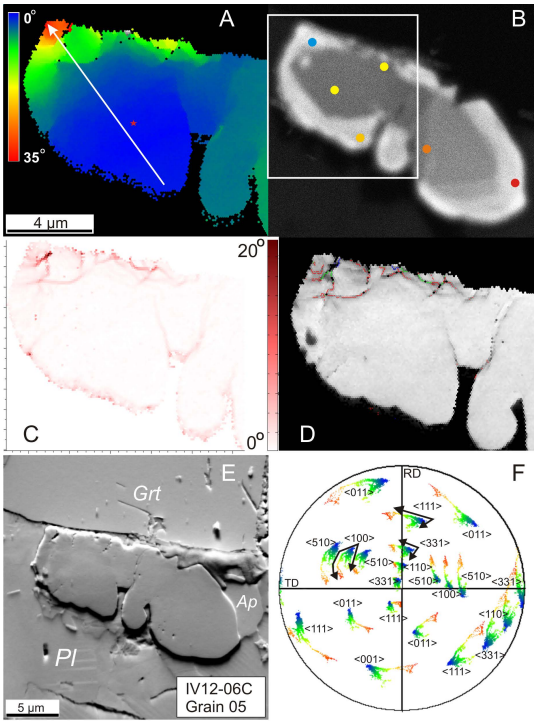

Figure 10. Grain IV12-06C_05. **(A)** EBSD map color coded for zircon misorientation with respect to a reference point (red star marker), the white arrow corresponds to the misorientation profile shown in Fig. 13b; **(B)** CL image, colored points represent relative degree of crystallinity, color coding as in Fig. 2b, the EBSD map position is marked by the white rectangle; **(C)** EBSD map of zircon showing the misorientation between neighboring data points; **(D)** EBSD pattern quality map with subgrain boundaries color-coded as in Fig. 8c; **(E)** FSE image, Grt = garnet, Pl = plagioclase, Ap = apatite; **(F)** pole figure plot showing zircon crystal directions (lower hemisphere equal area projection) colored as in **(A)**. Labels indicate the crystallographic directions. Black arrows indicate split in the direction of axes rotation.

SED
6, 1799–1861, 2014

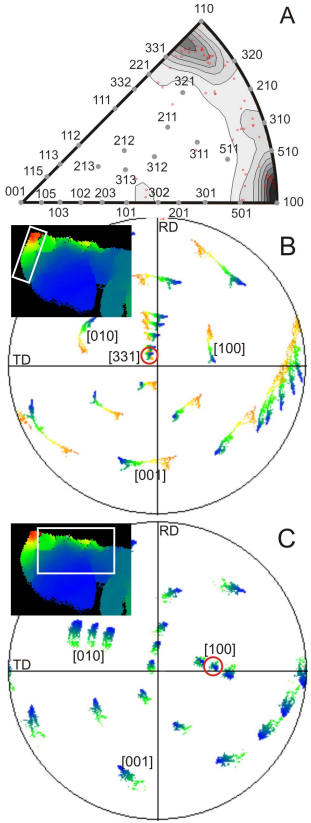

Figure 11. Orientation and misorientation data of grain IV12-06C_05. **(A)** Inverse pole figure plot of the misorientation axes distribution density, showing axes concentrated parallel to Zrn [331] and Zrn [100]. **(B)** and **(C)** pole figure plot showing crystal directions (lower hemisphere equal area projection) of two deformed parts of the grain (indicated by a white rectangle in the inset), colored as in insets. Misorientation axes are highlighted by red circle.

SED
6, 1799–1861, 2014

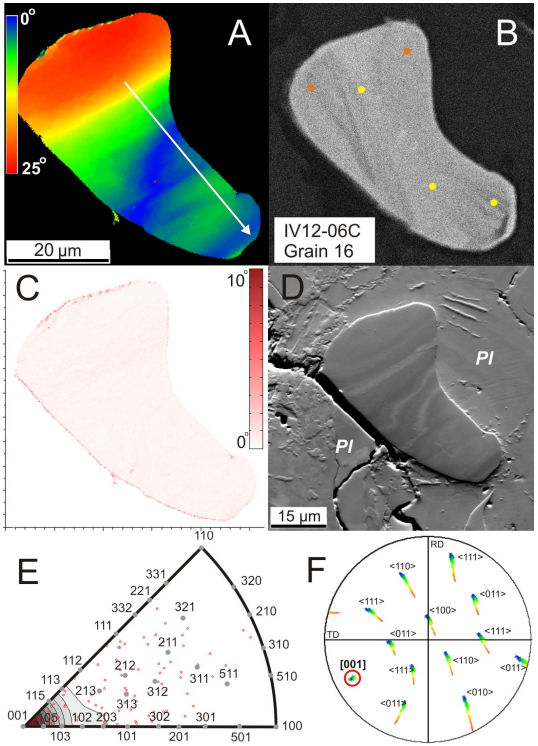

Figure 12. Grain IV12-06C_16. **(A)** EBSD map color coded for zircon misorientation with respect to a reference point (red star marker), the white arrow corresponds to the misorientation profile shown in Fig. 13a; **(B)** CL image, colored points represent relative degree of crystallinity, color coding as in Fig. 2b; **(C)** EBSD map of zircon showing the misorientation between neighboring datapoints; **(D)** FSE image, Pl = plagioclase; **(E)** inverse pole figure plot of the misorientation axes distribution density; **(F)** pole figure plot showing zircon crystal directions (lower hemisphere equal area projection) colored as in **(A)**. The red circle indicates rotation axis.

SED
6, 1799–1861, 2014

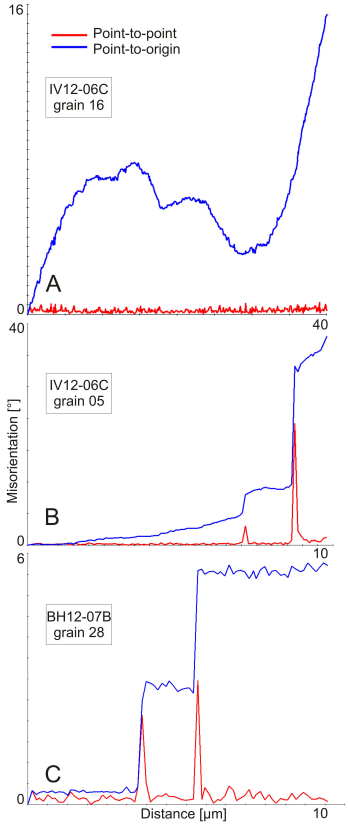

Figure 13. Misorientation profiles of zircon showing point-to point (red line) and point-to-origin (blue line) misorientations for **(A)** grain IV12-06C_16 displaying spatially continuous lattice rotation (for location of the profile line see Fig. 12); **(B)** grain IV12-06C_05, showing subgrain boundary formation together with spatially continuous lattice distortion (for location of the profile line see Fig. 10a); **(C)** grain BH12-07B_28 exhibiting subgrain formation (for location of the profile line see Fig. 4a).

SED
6, 1799–1861, 2014

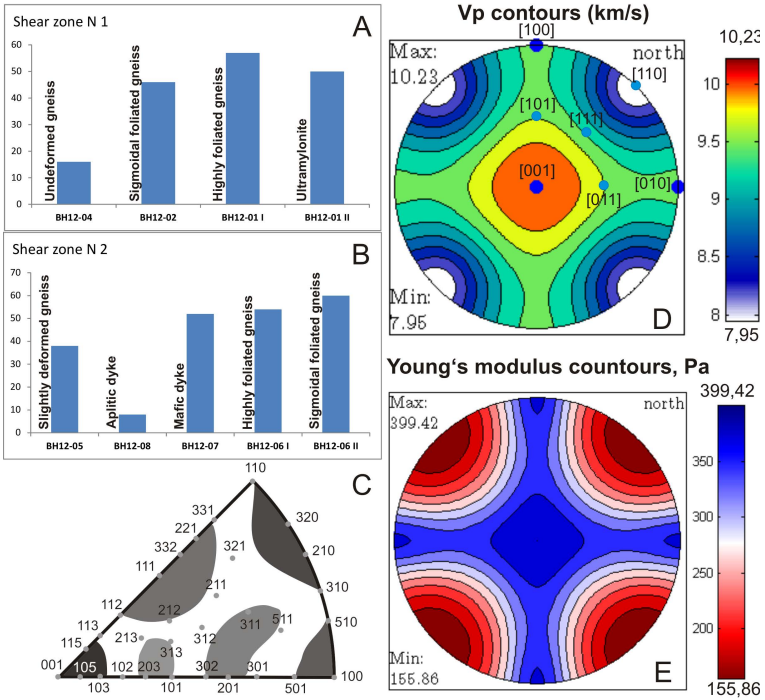

Figure 14. (A) Histogram, representing the percentage of deformed zircon grains in each sample of the profile across shear zone No. 1. The succession of rocks is from less deformed to mylonitized. **(B)** Histogram, representing the percentage of deformed zircon grains in each sample of the profile across shear zone No. 2. The succession of the rocks is equivalent to Fig. 1b, **(C)** Collective misorientation axes distribution density plot, based on 60 analyzed grains from different lithologies. The intensity of the color is proportional to the misorientation axes density. **(D)** and **(E)**: visualization of elastic properties of zircon by MTEX, elastic constants after Bass (1995). **(D)** *P* waves velocity; blue dots with labels indicate main crystallographic directions in zircon. **(E)** Young's modulus contours.

SED
6, 1799–1861, 2014

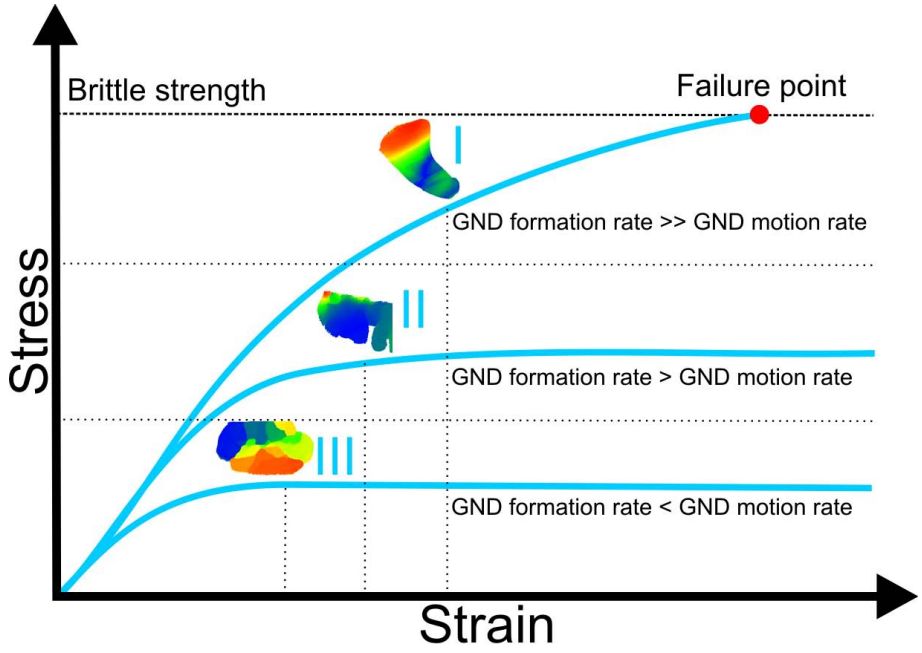

Figure 15. Stress/strain curves for different finite crystal-plastic deformation patterns in zircon. Curves I–III reflect deformation patterns type (I), (II) and (III) correspondingly. GND = geometrically necessary dislocations.

SED
6, 1799–1861, 2014